Capturing Animation-Ready Isotropic Materials Using Systematic Poking

HUANYU CHEN, University of Southern California, USA
DANYONG ZHAO, University of Southern California, USA
JERNEJ BARBIČ, University of Southern California, USA

Capturing material properties of real-world elastic solids is both challenging and highly relevant to many applications in computer graphics, robotics and related fields. We give a non-intrusive, in-situ and inexpensive approach to measure the nonlinear elastic energy density function of man-made materials and biological tissues. We poke the elastic object with 3d-printed rigid cylinders of known radii, and use a precision force meter to record the contact force as a function of the indentation depth, which we measure using a force meter stand, or a novel unconstrained laser setup. We model the 3D elastic solid using the Finite Element Method (FEM), and elastic energy using a compressible Valanis-Landel material that generalizes Neo-Hookean materials by permitting arbitrary tensile behavior under large deformations. We then use optimization to fit the nonlinear isotropic elastic energy so that the FEM contact forces and indentations match their measured real-world counterparts. Because we use carefully designed cubic splines, our materials are accurate in a large range of stretches and robust to inversions, and are therefore "animation-ready" for computer graphics applications. We demonstrate how to exploit radial symmetry to convert the 3D elastostatic contact problem to the mathematically equivalent 2D problem, which vastly accelerates optimization. We also greatly improve the theory and robustness of stretch-based elastic materials, by giving a simple and elegant formula to compute the tangent stiffness matrix, with rigorous proofs and singularity handling. We also contribute the observation that volume compressibility can be estimated by poking with rigid cylinders of different radii, which avoids optical cameras and greatly simplifies experiments. We validate our method by performing full 3D simulations using the optimized materials and confirming that they match real-world forces, indentations and real deformed 3D shapes. We also validate it using a "Shore 00" durometer, a standard device for measuring material hardness.

CCS Concepts: • **Computing methodologies** → **Physical simulation**.

Additional Key Words and Phrases: FEM, material, isotropic, optimization, palpation, force meter, durometer, laser
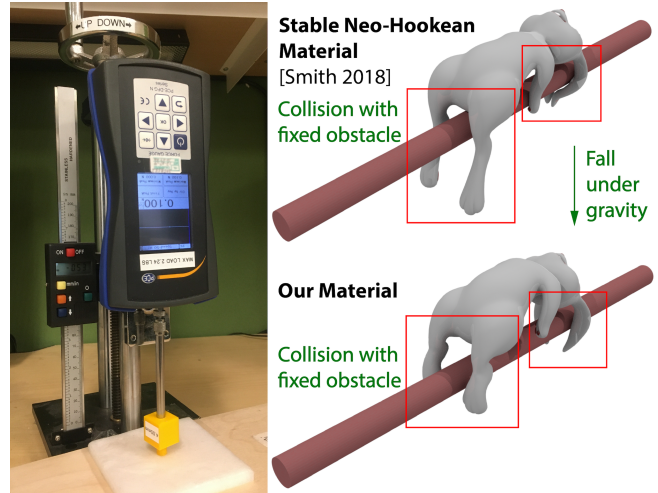
Fig. 1. **Measuring an elastic foam material via poking.** Left: Our experimental setup to measure the contact forces and indentations. The force stand has an LCD screen displaying the vertical translation in millimeters. The force meter to measure the contact force is mounted into the force stand. The rigid yellow poking cylinder (radius=4.05mm) and the poked foam specimen are visible at the bottom. Right: The measured elastic material is used for simulation. The bunny is dropped under gravity against a hard obstacle. The simulation results in the top and bottom image were obtained by fitting the best "Stable Neo-Hookean Material" (SNH) [Smith et al. 2018] and our generalized Neo-Hookean Material, respectively, to the measured foam forces and indentations. Real foam stiffens when stretched (Figure 17); and our material captures that; this produces less distortion in rabbit's legs and hands. We also tried increasing the gravity by 50%, and our material remained stable whereas the SNH material exploded. We investigate this stability further in Figure 9. This experiment demonstrates that our fitted materials not only match the force vs indentation data, but are also stable and suitable for computer animation applications.

1 INTRODUCTION

Realistic simulation of three-dimensional elastic solids is one of the key goals in computer animation, with applications in film, virtual reality, medicine, CAD/CAM and material science. In order to

Authors' addresses: Huanyu Chen, University of Southern California, Los Angeles, USA, huanyuc@usc.edu; Danyong Zhao, University of Southern California, Los Angeles, USA, danyongz@usc.edu; Jernej Barbič, University of Southern California, Los Angeles, USA, jnb@usc.edu.

succeed at such realistic simulation, there are a few essential ingredients: good timestepping, constraints and contact modeling, and accurate materials. While arguably great progress has been made on aforementioned problems, accurate nonlinear material modeling still remains challenging. The difficulty lies in that even in the arguably simplest nonlinear model, namely the isotropic materials, materials are modeled by elastic energy density functions that are symmetric functions of three variables, $\psi : \mathbb{R}^3 \mapsto \mathbb{R}$, and the space of all such functions is vast and difficult to parameterize, let alone fit to some real-world observations. The problem is compounded by the fact that in order to even setup such measurements, the elastic solid geometry must be known exactly, and the applied forces, their spatial distributions, and the boundary conditions such as fixed attachments must also be known exactly. These conditions are simply

not satisfied in most practical scenarios: forces do not apply at point locations, but spatially distribute in complex patterns; geometric shape deviates from the computer model already in the rest shape; and real-world attachments do not apply exactly at the modeled locations, and may even slide. Many real-world elastic objects also cannot be extracted from their natural environments without permanent damage. The challenge is then how to set up a controlled experiment so that the isotropic function ψ can be recovered from some easily performed non-destructive measurements.

In our paper, we give such a method to fit ψ to real-world observations, under the assumption that the material is isotropic and locally homogeneous. Our method stems from the observation that people have been judging the "stiffness" of objects for centuries by poking into them with fingers or other tools ("palpation"). We make this intuitive method precise by setting up controlled experiments where the "poking" and the resulting contact forces are systematically controlled and measured (Figure 1). In order to make the boundary conditions and the geometry predictable, we poke thin layers of material that are positioned on top of a hard rigid surface, and that have a known finite depth, but that extend large distances (for all practical purposes "infinitely") in the other two directions. To control the contact force distribution, we poke the elastic material with several rigid cylinders of known small radii. Because the cylinder radii are small and the deformations are localized, such measurements are reasonably accurate even if the extent is not "infinite" and even if the surface is not perfectly planar (Figure 21). Our method is inexpensive to use because it relies only on a force sensor and 1D indentation (displacement) data, and does not need computer vision equipment, or capturing surface or volumetric displacement data. Thanks to our untethered laser-based setup, it also does not require extracting or damaging the specimen, which is instead investigated in its natural environment.

The space of all isotropic functions ψ is infinite and must be somehow parameterized. Multiple standard families have been proposed in literature, such as co-rotational, St.Venant-Kirchhoff and Neo-Hookean materials [Bonet and Burton 1998]. These materials, however, only have two parameters, which is insufficient to capture real materials under large deformations. Instead, we adopt a stretch-based Valanis-Landel family of materials [Valanis and Landel 1967; Xu et al. 2015] whereby we model arbitrary dependence of tensile stiffness vs strain using a univariate natural cubic spline, plus volume compressibility. As such, our materials lessen inductive bias commonly present in material optimizations in literature. Our material family is a generalization of the Neo-Hookean material. It inherits its linearization properties under small deformations whereby all isotropic materials "collapse" into a 2-dimensional family of materials, but, unlike the Neo-Hookean material, permits controlling stiffness under large deformations. We note that a similar Valanis-Landel material has been used in engineering literature to fit rubber-like *incompressible* materials [Sussman and Bathe 2009]. Unlike prior work, our method can estimate volume compressibility (Poisson's ratio) and model compressible materials (ranging from $\nu = 0$ to $\nu = 0.495$ in our examples), which is important in practice as many real material are compressible. Our material family contains the Neo-Hookean material [Bonet and Burton 1998] as as a special case. It also includes other popular families of materials, such as the
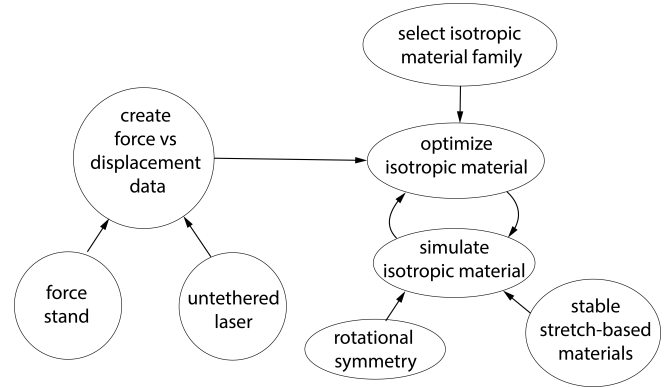
Fig. 2. **Overview.** The force vs indentation curves are experimentally determined either via a force stand (Figure 1), or a laser (Figure 3); in both cases paired with a force meter. We propose a new isotropic material family (Section 6) that subsumes many common materials, and optimize within it for a material best matching the force vs indentation curves (Section 7). The optimization employs simulation as an inner loop, and this is made fast by exploiting rotational symmetry (Section 4.1), and stable by proposing an improved theory of stretch-based materials (Section 5).

Hencky's material [Neff et al. 2016], STS material [Pai et al. 2018] and the Ogden material [Ogden 1972] (these materials are given in Appendix A). Also note that our method permits estimation of the familiar Lamé parameters or, equivalently, Young's modulus and Poisson's ratio.

Before we could optimize our Valanis-Landel family, we observed that existing *stretch-based* simulation literature [Valanis and Landel 1967; Xu et al. 2015; Zhu 2021] does not address the simulation singularities that occur when two or three stretches become equal, or the indefiniteness of the tangent stiffness matrix. We give a solution to this problem for stretch-based materials, including a method to project stretch-based materials to positive-definiteness. Stretch-based materials are materials whereby the elastic energy function is expressed directly as an isotropic function of the principal stretches $\lambda_1, \lambda_2, \lambda_3$ of the material, as opposed to via *invariants* computed from the principal stretches [Smith et al. 2019]. As observed in prior work [J.M.Ball 1984; Zhu 2021], the Hessian of the elastic energy density of a stretch-based materials conveniently diagonalizes in a properly selected basis. In addition to dealing with singularities, we give a complete exposition of the diagonalization fact that includes both an explicit statement of the basis (mirroring [Smith et al. 2019]) and the Hessian diagonal blocks (mirroring [J.M.Ball 1984; Zhu 2021]), as well as proofs that the diagonalization is independent of the basis choice in case of singularities. Such complete treatment of stretch-based materials does not appear in any prior reference. As such, while the focus of our work is material optimization, our work also has a contribution to stretch-based material simulation.

We note that there exists standardized [International 2021] equipment for measuring the "hardness" of materials (the "Shore" value) via poking, namely the *durometer* (Figure 24, d). The durometer, however, only produces a single value which obviously cannot subsume the entire nonlinear elastic behavior, whereas in our work, we recover a detailed ψ function. We achieve this by poking the

elastic material with rigid cylinders and continuously measuring the indentation and the contact force. We then optimize the univariate natural cubic spline control points of our ψ to match these recorded indentations and contact forces. Crucially, we poke the material with several rigid cylinders with different radii, which enables us to capture volume-preservation material characteristics, in addition to tensile stiffness. In order to perform the optimization, we model the elastic object using the Finite Element Method. We found that in order to meet any reasonable accuracy (e.g., under 10% error), very detailed computational meshes are required, and this is intractable if applied naively. Instead, we demonstrate how to exploit the radial symmetry of the problem to convert 3D FEM simulations into equivalent 2D FEM simulations that produce identical 3D elastic energy and elastic forces, but that can be executed orders of magnitude faster. This makes our optimizations tractable and enables us to produce ψ functions that match real-world observations. An overview of our method is given in Figure 2. We perform an extensive evaluation of our work (Figure 9, Figure 11, Figure 23, Figure 24, Figure 29, Section 8.5, Section 8.10).

2 RELATED WORK

2.1 Capturing elastic materials

Simulating elastic objects has been an active field of research in computer graphics for many decades. A diverse range of elasticity models has been used extensively, such as StVK [Bonet and Burton 1998], linear corotational [Müller and Gross 2004], Neo-Hookean [Treloar 1944], among others. Recent efforts have focused on acquiring materials that faithfully replicate the physical properties of real-world counterparts, while maintaining computational stability suitable for computer graphics applications.

To obtain a realistic material, one approach is to choose a material model and then fine-tune the parameters based on empirical data. Xu et al. [Xu et al. 2015], for instance, introduced a spline-based material model that allows artists to design materials interactively. Nevertheless, this process can be extremely tedious and inefficient, particularly when dealing with a large parameter space. An alternative approach is to interact with real-world materials, record their responses, and use the data to estimate the material parameters. In the 2000s, researchers in medical engineering have determined Young's moduli and Poisson's ratios of soft tissues via indentation tests. They have either pre-assumed Poisson's ratio [Zhang et al. 1997], or measured it through a separate experiment [Jurvelin et al. 1997]. Early in computer graphics, [Lang et al. 2002; Pai et al. 2001] modeled linear elasticity on 3D models using a matrix representation of Green operators, and fitted the matrix with force and displacement data, where the latter was captured using a trinocular stereo vision system. Becker et al. [Becker and Teschner 2007] proposed a method to fit Young's moduli and Poisson's ratios, but required displacement data for all vertices. Sussman et al. [Sussman and Bathe 2009] estimated nonlinear incompressible materials via uniaxial tensile tests, but assumed homogeneity in material deformation, which is often not the case.

When dealing with models that incorporate nonlinearity, anisotropy, heterogeneity, or friction, analytical estimation formulas become infeasible. Instead, data-driven or simulation-driven methods offer compelling alternatives. These methods typically recast parameter estimation as an inverse optimization problem. They iteratively simulate the interactions using FEM to compute mechanical quantities of interest and update material parameters, until the difference between measured and simulated quantities is minimized. Volumetric solids have been measured through indentation tests [Bickel et al. 2010, 2009; Pai et al. 2018], cloth has been measured through biaxial tensile tests [Miguel et al. 2012, 2013; Wang et al. 2011], and through video [Bhat et al. 2003; Yang et al. 2017], and dynamic trajectories have been measured through spacetime optimization [Wang et al. 2020, 2015]. Recently, an approach was proposed to estimate material properties of elastic solids using depth sensors [Arnavaz et al. 2023]. They use the Stable Neo-Hookean material [Smith et al. 2018] (only 2 parameters) to which we compare extensively. These methodologies often rely on costly devices, complex measuring systems, or intricate data processing procedures. Moreover, tensile tests require the extraction of material samples from their natural environments. In contrast, we recover nonlinear isotropic material functions of hyperelastic volumetric solids via indentation tests without any cameras or vision systems, and do so in-situ, i.e., without damaging or extracting the physical specimen from its natural environment.

In haptic rendering applications, a hand-held probe device that can measure both contact force and acceleration simultaneously [Pai and Rizun 2003] was proposed to measure the haptic texture of a stiff object. Data-driven methods are also widely used in measuring deformable objects [Sianov and Harders 2013; Yim et al. 2016], by using devices that can record both positions and forces over time. Nonlinear elastic properties have also been captured [Bickel et al. 2009; Pai et al. 2018]. However, these previous applications fitted nonlinear materials that are described by a small number of parameters. Our materials use an arbitrary number of parameters to model complex nonlinear materials under large deformations.

2.2 Boussinesq contact approximations

In contact mechanics, Boussinesq approximations [Sneddon 1946] are a popular approach to modeling the relationship between the deformations and stresses that occur when a halfspace made of elastic material is poked with a rigid indenter. Boussinesq approximations assume that the material is linear and deformations small, and then analytically solve the Naviér elasticity equations for certain simplified geometric setups. For example, the relationship between the deformation of an infinite-width infinite-depth 3D half-space and the contact force distribution against a point contact or circular contact has an analytical solution [Johnson and Johnson 1987], and this has been exploited in previous work [Harmon and Zorin 2013; Pauly et al. 2004]. For infinite width but finite depth, the relation between the deformation of a circular contact area and its contact force is also known to have a numerical solution [La Ragione et al. 2008]. The distribution of stress and deformation have also been modeled for composite materials [Peutz et al. 1968]. All of these methods assume both material linearity and small deformations, whereas in our work we model *nonlinear* materials and *large* deformations. Because there are no analytical solutions to the nonlinear PDEs of elasticity, we use FEM to model our deformations and contact forces.

2.3 Nonlinear material modeling

One of the major challenges of simulation-driven methods lies in selecting an appropriate material model. In terms of nonlinear material models, Pai et al. [Pai et al. 2018] used a 3-parameter model. Stress-strain relationships were interpolated using radial basis functions [Bickel et al. 2010, 2009; Wang et al. 2020]. Problematically, the resulting interpolated elastic forces were non-conservative. Miguel et al. [Miguel et al. 2016] suggested a model that interpolates the elastic energy density function ψ. Enforcing the convexity condition for their material proved challenging, and their parameter fitting suffered from local minima [Miguel et al. 2016]. Our optimizer differs from that of [Miguel et al. 2016] in that we employ a "Fit E" step that optimizes for the overall materials at the beginning of each iteration, and this is shown to significantly accelerate convergence (Section 7).

An ideal material model needs to be expressive enough to accommodate a variety of behaviors while excluding redundant and unstable materials. Numerous nonlinear models written in terms of invariants are available [Wex et al. 2015], such as Mooney-Rivlin [Mooney 1940; Rivlin 1948], Yeoh [Yeoh 1990, 1993], Fung-Demiary [Demiray 1972; Fung 1967], Veronda-Westmann [Veronda and Westmann 1970], Gent [Gent 1996] and Arruda-Boyce [Arruda and Boyce 1993] materials, and have been used in [Kauer et al. 2002; Kim and Srinivasan 2005; Schumacher et al. 2020]. Nevertheless, they either have too few parameters, or their convexity conditions are difficult to enforce. Stretch-based material models, such as Ogden materials [Clyde et al. 2017; Ogden 1972] and Valanis-Landel materials [Valanis and Landel 1967], offer some promise to ensure convexity. Clyde et al. [Clyde et al. 2017] introduced an Ogden-like separable energy for fabrics and cloth based on orthotropic strain components, but did not discuss convexity conditions. Valanis-Landel model offers a simple, easy to enforce convexity condition, and has been used to fit incompressible materials [Sussman and Bathe 2009]. Xu et al. [Xu et al. 2015] proposed a compressible Valanis-Landel model, with three univariate functions for control, and all of them being convex yields polyconvexity of the material itself, which is easy to enforce. In our work, we use a simplified version of this compressible Valanis-Landel material model, in order to circumvent ambiguities and overly large parameter spaces. However, convexity alone may not be sufficient; the linear corotational material is convex with respect to any combination of stretches (including negative ones), yet it has proven unstable [Stomakhin et al. 2012], in that elements can readily invert and fail to recover. The ability for elements to recover from inversions is crucial, as inversions are common, sometimes even inevitable, in computer graphics due to discretization and numerical instabilities [Stomakhin et al. 2012]. We demonstrate in our paper that our fitted generalized Neo-Hookean materials have good invertibility properties (Figure 9).

The stabilization of existing materials is another intriguing research area. For instance, Smith et al. [Smith et al. 2018] proposed a stabilized Neo-Hookean material, while [Stomakhin et al. 2012] stabilized random material functions through extrapolation. In material fitting, it is very important to accommodate stretches or strains that are outside the experimental region, but very few works dealt with this. Clyde et al. [Clyde et al. 2017] extended their fabric material model to region outside of experimental strain space via C2 extrapolation, but because they relied on the Ogden material, they did not have stability guarantees. Our material model is designed using carefully crafted cubic splines that inherently stabilize the material. We prove stability via stress tests (Figure 9), ensuring that any of our fitted materials are directly applicable for computer graphics applications.

2.4 Block-diagonal structure of element stiffness matrix

Another limiting factor in simulation-driven methods is the simulation process itself. Once a material model is established, it is necessary to robustly and efficiently simulate any material instance from the model to thoroughly explore the material space. Recently, many publications have focused on developing differentiable simulators [Geilinger et al. 2020; Jatavallabhula et al. 2021; Le Lidec et al. 2021; Liang et al. 2019], facilitating inverse optimization of more complicated dynamic systems [Hahn et al. 2019; Kandukuri et al. 2020; Sengupta et al. 2020; Song and Boularias 2020].

Our focus is on elastostatic FEM simulations, which typically involve computing force and the tangent stiffness matrix. Early works in medical engineering [Choi and Zheng 2005; Kim and Srinivasan 2005; Zhang et al. 1997] relied on FEM software from industry. Many previous works in computer graphics [Bickel et al. 2010, 2009; Wang et al. 2015] relied on linear corotational FEM, which is unsuitable for simulating general nonlinear materials. Miguel et al. [Miguel et al. 2016] calculates force and stiffness matrix through finite-differencing, which demands substantial computational effort. For isotropic materials, forces can be readily calculated through the first Piola-Kirchhoff tensor [Irving et al. 2004]. However, the tangent stiffness matrix requires more effort. This involves computing the Hessian of the energy density function with respect to deformation gradients, followed by projection to the semi-positive definite (SPD) space. Such SPD matrices also play a critical role in geometric optimization, enabling the derivation of a second-order solver to optimize distortion energies with Newton-type convergence, with applications across numerous problems including mesh parameterization [Chen and Weber 2017; Fu and Liu 2016; Fu et al. 2015; Liu et al. 2018; Shtengel et al. 2017; Smith et al. 2019; Smith and Schaefer 2015; Zhu 2021]. To compute the tangent stiffness matrix, [Teran et al. 2005] unveiled a block-diagonal structure in the element stiffness matrix of upper invariants-based energies, comprising one 3x3 block and three 2x2 blocks. This formula was extended by [Stomakhin et al. 2012] to accommodate stretch-based energies. A different method for stretch-based energy, through differentiating the singular value decomposition (SVD), was introduced by [Xu et al. 2015]. Smith et al. [Smith et al. 2019] focused on lower invariant-based energies, discovering that the block-diagonal structure can be further simplified to one 3x3 block and 6 diagonal entries, with all 9 eigenvalues extractable for some energies. The basis was also presented in a simple form. Later, Zhu [Zhu 2021] derived the same structure for stretch-based energies and expressed the basis as a product of several matrices, resulting in the same basis as [Smith et al. 2019]. Generally, stretch-based energy models present simpler eigenvalue forms compared to invariants based energies, but often encounter singularities when two stretches are nearly equal. Xu

et al. [Xu et al. 2015] suggested a workaround by perturbing the stretches to increase their difference, but this approach is imperfect. Instead, we demonstrate that all singularities are removable and give a method for removing them using Taylor series (Appendix C and Appendix D). This contribution makes stretch-based materials suitable for general robust use in computer graphics.

3 CAPTURING CONTACT FORCES AND INDENTATIONS

We systematically poke the elastic object with rigid cylinder of various radii, measuring the relationship between indentation and the total contact force. By "indentation", we mean the vertical distance between the contact site at the bottom of the cylinder, and the undisturbed height of the elastic object far from the contact site (depicted as d in Figure 4). We measure the total contact force using a force meter "PCE-DFG N 10" from PCE Instruments (resolution is 0.005N; Figure 1). The 3d-printed rigid hard-plastic cylinder is attached to the force meter's tip using M6 screws with 3d-printed holes for screw threads. The radii for our cylinders vary from approximately 1mm to 5mm. The acquisition of force values is automatic via connecting the force meter's digital output to a DAQ card.

We use two methods to measure indentation. For objects that are small and unattached (or can be manufactured as such, as is the case with chemistry-based manufacturing of foams and silicons), we put the force meter into a force stand (also from PCE Instruments; Figure 1), and position the specimen to be examined at the bottom of the stand. We then slowly and precisely lower the force meter using the precision wheel and thus acquire the indentation and forces. The vertical position of the force meter can be read on the force stand LCD screen; resolution is $10\mu m$.

The limitation of the force stand is that it is heavy and not portable. For objects that cannot be practically cut into layers and positioned into the force stand, such as a chair cushion or human body parts, we propose a novel laser-based instrument (Figure 3). This permits us to perform in-vivo measurements of the human tissue. We use the Optex-CD22-100 laser distance measurement sensor with a resolution of $20\mu m$. The acquisition of laser distance values is automatic via connecting the laser's digital output to the DAQ card. We mount both the force meter and the laser onto a 3d-printed plastic (Tough PLA) frame, in a manner where the laser's optical axis is parallel to the force meter axis. The parallelism of the two axes can be achieved via a calibration step whereby one attaches the laser frame into the force stand, rotate the force stand wheel, and compares the distance values of the laser to those read on the force stand's LCD display. The angle of the laser can then be adjusted via a pivot joint on the laser frame until both the force stand and laser report equal translations. Our crucial observation is that laser must be mounted in a manner whereby the parallel distance between the force meter axis and the laser axis is sufficiently large so that the point illuminated by the laser does not deform (Figure 4). This (perhaps somewhat surprisingly) makes it possible to measure indentation, as the laser is now effectively directly measuring the global world-coordinate vertical translation of the force meter housing. Because the force meter internally operates as a force sensor (without any springs), the rigid cylinder mounted onto the force meter moves rigidly with the force meter housing. This means that the indentation equals the difference of the laser distance at the first onset of contact, and the current laser distance (Figure 4, middle). Our laser frame has a translational joint to adjust the distance of the laser and force meter axes to ensure that the parallel distance is sufficiently large; but we rarely needed to adjust it in practice beyond the initial setting. We are not aware of anyone proposing such a one-dimensional laser-based force vs indentation measuring device, and we think our idea is applicable broadly in applications such as haptics. Note that for untethered styluses in haptics, existing designs [Zamani and Culbertson 2022] typically employ a magnetic sensor to sense positions, which is at least an order of magnitude less precise as our laser-based instrument.

Regardless of the distance tech employed (force stand or laser), we poked each examined material with rigid cylinders of various radii. The deepest indentation was approximately 20% of the total depth of the material layer, which is deeply in the nonlinear material region. The zero indentation is determined to be the moment when the force meter first registers a non-zero value, i.e., at the onset of contact. We typically acquire ~10 (indentation, force) data pairs, with the maximum force typically at around $\sim 5N$ (maximum force of our force meter is $10N$). We apply a smoothing filter to all acquired signals. To increase the contact force accuracy, we repeat the entire poking sequence 3 times, and use the average contact force at each indentation. Our experimental setup is relatively inexpensive, as our laser and force meter only cost $750 and $800, respectively. Note that our setup gives very high positional accuracy, but does not require any optical cameras or mocap markers, which alone can cost more than $10,000 for comparable accuracy; as such, our system is a relatively inexpensive approach to acquiring isotropic materials.

4 ELASTOSTATIC SIMULATION

In order to fit the isotropic elastic energy density function Ψ to the poking data captured in Section 3, we need to build a digital twin of our elastic material layer. We do this using FEM simulation, augmented with constraint handling to accommodate contact with the rigid cylinder. We assume an isotropic strain-stress law in the material, and model it using a symmetric elastic energy density function $\Psi(\lambda_1, \lambda_2, \lambda_3) : \mathbb{R}^3 \to \mathbb{R}$, where λ_i are the three singular values (the "principle stretches") of the 3×3 deformation gradient F of the elastic deformation [Irving et al. 2004]. Symmetry here means that $\Psi(\lambda_1, \lambda_2, \lambda_3) = \Psi(\lambda_2, \lambda_1, \lambda_3) = \Psi(\lambda_1, \lambda_3, \lambda_2) = \Psi(\lambda_3, \lambda_2, \lambda_1)$. We will further restrict our Ψ later in Section 6; but the discussion in this Section 4 is generic with respect to any isotropic Ψ.

4.1 Cylindrical Coordinates and Axial Symmetry

We first attempted to model the elastic layer using a 3D mesh and 3D FEM simulation; but this turned out to be orders of magnitude too slow to perform our optimization. To accelerate the simulation and the material optimization, we invented a technique to replace 3D simulation with a 2D simulation that produces mathematically identical results (modulo numerical errors). We assume that the object deforms locally in response to the poking; therefore, we can approximate the elastic layer as quasi-infinite in tangential directions, and having a certain constant finite depth. We do not assume
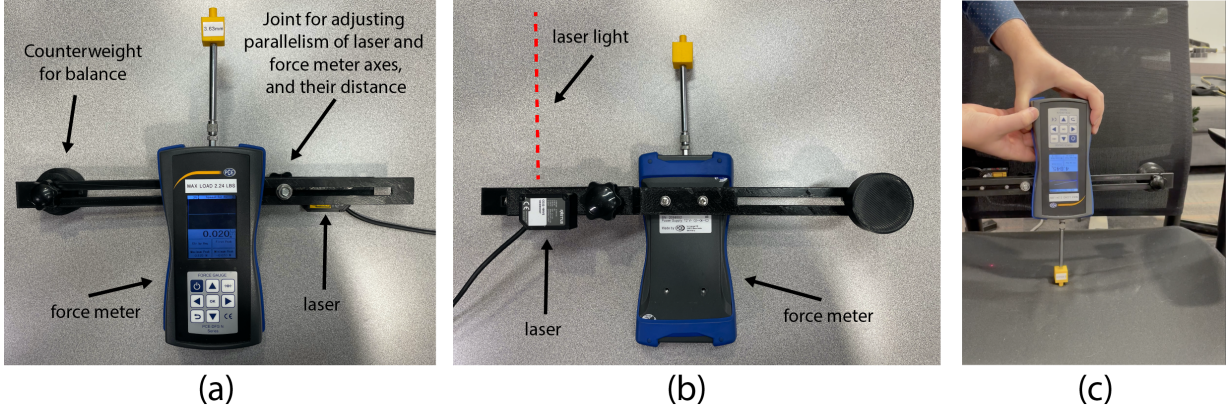
Fig. 3. **Laser and force meter for measuring indentation and contact forces.** (a,b) Front and back of the laser instrument, showing the laser, force meter and the plastic frame with joints for adjusting laser vs force meter axis parallelism and axis parallel distance. The large black circular object is a counter-weight for easier balance against the weight of the laser. (c) The instrument in action when measuring the material of a chair seat. The red laser light is visible, and is positioned far from the contact site, as required. Although others have poked soft tissues before in computer graphics [Bickel et al. 2009], they typically paired a force sensor with a vision system. The novelty of our system is to pair a force sensor with a 1D laser system, which is both significantly more precise and cheaper than a vision-based deformation capture rig (precision down to a few micrometers for under $1000).
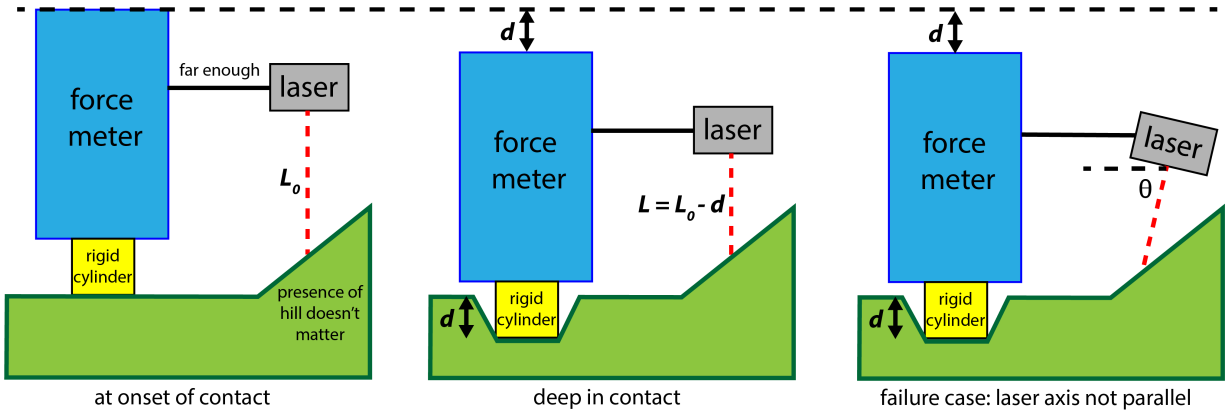

Fig. 4. **Using a laser to measure indentation.** Left: we store the laser distance L_0 at onset of contact, i.e., the moment of time when the force meter changes from zero force to non-zero force. It does not matter if the laser is shining on a bump or a slope, as long as laser is sufficiently far away to not shine on the contact deformation region. The entire device should be kept orthogonal to the surface for accurate data collection. Middle: the indentation d can be calculated from L as $d = L_0 - L$. Right: laser and force meter axes must be parallel. Any non-parallelism introduces no indentation error at the onset of contact; namely, due to $L = L_0$, we correctly detect $d = 0$. Suppose the laser is shining at an angle θ close to $90°$, but not exactly $90°$. Then, the relative error in the measured indentation $d = L_0 - L$ is $1 - sin(\theta)$. At $\theta = 80°$ (i.e., $10°$ error), this is only 1.5%, and at $\theta = 85°$ (i.e., $5°$ error), this is only 0.4%.

small deformations; and actually, it is necessary to excite the material to large deformations to recover the nonlinear elastic material. We poke the elastic material with a rigid cylinder in a normal direction. We assume that the material is locally homogeneous close to the poking site. Under these assumptions, the deformation and the contact force are axis-symmetric and there is no deformation in the angular direction, which we can exploit for simulation speed, as follows. We use a cylindrical coordinate system (r, φ, z); the deformation and contact force are independent on φ. Figure 5 illustrates how we can substitute a 3D cylinder mesh for a 3D rectangle grid, by exploiting symmetry. The total 3D elastic energy can be written as

$$
\begin{aligned}
\mathcal{E} &= \int_\Omega \Psi(\lambda_1(F), \lambda_2(F), \lambda_3(F)) dV \\
&= \int_0^{2\pi} d\varphi \int_0^h \int_0^R \Psi(\lambda_1(F), \lambda_2(F), \lambda_3(F)) r \, dr \, dz \\
&= 2\pi \int_0^h \int_0^R \Psi(\lambda_1(F), \lambda_2(F), \lambda_3(F)) r \, dr \, dz.
\end{aligned} \tag{1}
$$

Although cylindrical coordinates are standard in FEM simulation [Comsol 2023], our contribution here is to demonstrate how to apply cylindrical symmetry to 3D force-indentation-based large-deformation FEM material optimization problems.
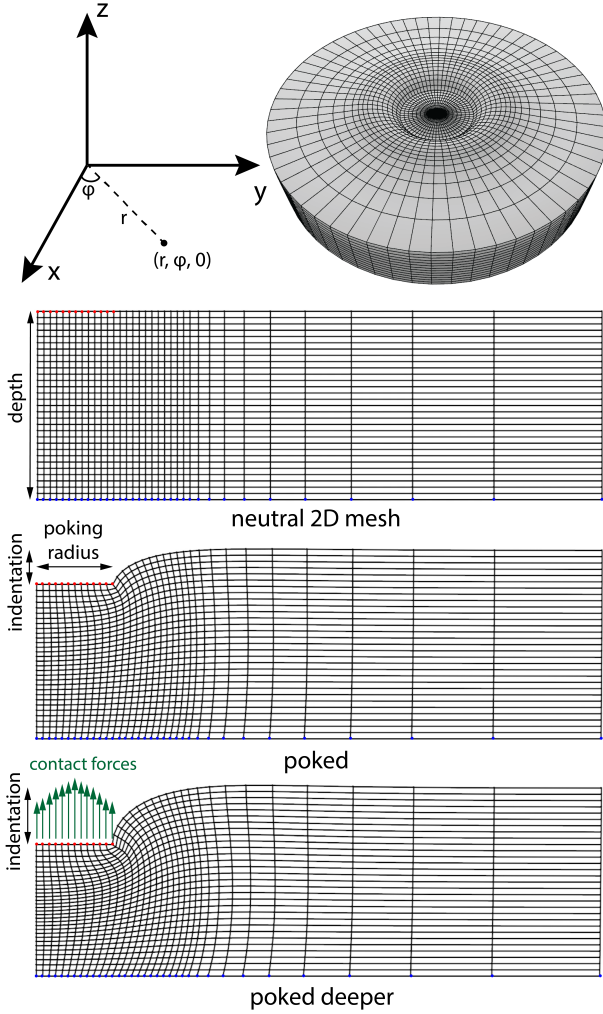
Fig. 5. **Simulation setup and radial symmetry:** Top: cylindrical coordinate system and the cylindrical 3D simulation mesh. Deformations are independent of φ. Bottom three pictures: 2D rectangular mesh, corresponding to a single (r, z) slice; we run our 2D FEM simulations on this mesh, using an elastic energy that exactly matches the 3D energy. We use Dirichlet displacement conditions under the cylinder (red; contact vertices), and at the bottom of the elastic material (blue; affixed to the ground). Simulations are quasi-static: we always find the static equilibrium of the deformable mesh under the given rigid cylinder indentation. In practice, we repeat the poking with cylinders of several different radii, which greatly helps with determining the material (analyzed further in Figure 11). The undeformed mesh is generated procedurally, based on parameters controlling the number of radial divisions under the rigid cylinder (typically 20 across the diameter). Vertical divisions are chosen so that elements under contact are squares (typically 30). Past a distance of radius away from contact, elements progressively lengthen based on a geometric series as the deformations become progressively more "boring" away from contact, requiring lesser precision. There are typically 60 elements across the mesh radial diameter.

4.2 Gauss Quadrature Points

Observe that the integration on φ has disappeared in the last line of Equation 1. Therefore, we can numerically evaluate the integral using a 2D rectangular mesh in the (r, z) space. To efficiently compute the elastic energy, its gradient and Hessian with respect to vertex positions (the elastic force and tangent stiffness matrix), we use Gauss points [Wriggers and Laursen 2006] to approximate the integral of the elastic energy. Inside each rectangular element, we sample 3x3=9 Gauss quadrature points. We experimented with schemes of other orders, and found the 3x3 lattice to be a good compromise between accuracy and computational speed. For example, when using 5x5=25 Gauss quadrature points, the output difference was negligible (relative output change of 1e-5). The integral of the elastic energy can be approximated as

$$\mathcal{E} = 2\pi w_k \sum_k \Psi(\lambda(F_k)) \, r_k, \tag{2}$$

where w_k is the weight of the Gauss quadrature point, and r_k is the radial coordinate of that point. The weights and positions are given in Appendix B.

4.3 2D Finite Element Method for the 3D Elastic Energy

Before we derive the elastic forces and tangent stiffness matrix, we need to first calculate the deformation gradient F_k at the Gauss points. For any location in the 3D solid cylinder, the deformation can be expanded in cylindrical coordinates as

$$u(r, \varphi, z) = \sum_i (u_i^r \cdot e_r + u_i^z \cdot e_z) \phi_i(r, z), \tag{3}$$

where (u_i^r, u_i^z) is the 3D deformation in any φ plane; $e_r = (\cos\varphi, \sin\varphi, 0)$ and $e_z = (0, 0, 1)$ are cylindrical basis vectors; $\phi_i(r, z)$ is the value of i-th FEM basis function at (r, z); and summation is over all FEM basis functions. We use bilinear interpolation to define shape functions ϕ_i; there is one shape function per vertex of the 2D mesh. Note that due to symmetry, shape functions ϕ_i are independent of φ, and u has no e_φ component. Now, we can calculate the deformation gradient as

$$F(x, y, z) = I_{3\times3} + \frac{\partial u(x, y, z)}{\partial(x, y, z)} =$$
$$= I_{3\times3} + \sum_i \frac{\partial\big((u_i^r \cdot e^r + u_i^z \cdot e^z)\phi_i\big)}{\partial(r, \varphi, z)}\left(\frac{\partial(x, y, z)}{\partial(r, \varphi, z)}\right)^{-1}. \tag{4}$$

Due to symmetry, we can set $\varphi = 0$, and therefore simplify

$$F_k(r_k, z_k) = I_{3\times3} + \sum_i \begin{bmatrix} u_i^r \dfrac{\partial\phi_i}{\partial r} & 0 & u_i^r \dfrac{\partial\phi_i}{\partial z} \\[2mm] 0 & u_i^r \dfrac{\phi_i}{r_k} & 0 \\[2mm] u_i^z \dfrac{\partial\phi_i}{\partial r} & 0 & u_i^z \dfrac{\partial\phi_i}{\partial z} \end{bmatrix}. \tag{5}$$

Observe that F_k can be divided into a 2×2 and a 1×1 submatrices. Thus, when computing the SVD of F_k, λ_3 is the matrix central element; and we only need to actually perform a 2×2 SVD to get λ_1 and λ_2. We can now compute the elastic force on a mesh vertex,

$$f = \frac{\partial\mathcal{E}}{\partial u} = 2\pi \sum_k \omega_k r_k \frac{\partial\Psi}{\partial u} = 2\pi \sum_k \omega_k r_k \frac{\partial\Psi}{\partial F}_{|F=F_k} \frac{\partial F_k}{\partial u}. \tag{6}$$

$$F = U \operatorname{diag}(\lambda_1, \ \lambda_2, \ \lambda_3) \ V^T$$

$$\frac{\partial \Psi}{\partial F} = U \operatorname{diag}(\partial_1 \Psi, \ \partial_2 \Psi, \ \partial_3 \Psi) \ V^T$$

$$\begin{cases} \mathbf{d}_1 = \operatorname{vec}(\mathbf{u}_1 \mathbf{v}_1^T) \\ \mathbf{d}_2 = \operatorname{vec}(\mathbf{u}_2 \mathbf{v}_2^T) \\ \mathbf{d}_3 = \operatorname{vec}(\mathbf{u}_3 \mathbf{v}_3^T) \end{cases}, \quad \begin{cases} \mathbf{t}_1 = \frac{\operatorname{vec}(\mathbf{u}_3 \mathbf{v}_2^T - \mathbf{u}_2 \mathbf{v}_3^T)}{\sqrt{2}} \\ \mathbf{t}_2 = \frac{\operatorname{vec}(\mathbf{u}_1 \mathbf{v}_3^T - \mathbf{u}_3 \mathbf{v}_1^T)}{\sqrt{2}} \\ \mathbf{t}_3 = \frac{\operatorname{vec}(\mathbf{u}_2 \mathbf{v}_1^T - \mathbf{u}_1 \mathbf{v}_2^T)}{\sqrt{2}} \end{cases}, \quad \begin{cases} \mathbf{l}_1 = \frac{\operatorname{vec}(\mathbf{u}_3 \mathbf{v}_2^T + \mathbf{u}_2 \mathbf{v}_3^T)}{\sqrt{2}} \\ \mathbf{l}_2 = \frac{\operatorname{vec}(\mathbf{u}_1 \mathbf{v}_3^T + \mathbf{u}_3 \mathbf{v}_1^T)}{\sqrt{2}} \\ \mathbf{l}_3 = \frac{\operatorname{vec}(\mathbf{u}_2 \mathbf{v}_1^T + \mathbf{u}_1 \mathbf{v}_2^T)}{\sqrt{2}} \end{cases}$$

$$B = [\mathbf{d}_1, \ \mathbf{d}_2, \ \mathbf{d}_3, \ \mathbf{t}_1, \ \mathbf{t}_2, \ \mathbf{t}_3, \ \mathbf{l}_1, \ \mathbf{l}_2, \ \mathbf{l}_3]$$

$$\frac{\partial^2 \Psi}{\partial F^2} = B \begin{bmatrix} \partial_{11}\Psi & \partial_{12}\Psi & \partial_{13}\Psi \\ \partial_{12}\Psi & \partial_{22}\Psi & \partial_{23}\Psi \\ \partial_{13}\Psi & \partial_{23}\Psi & \partial_{33}\Psi \end{bmatrix} \quad \cdots \quad B^T$$

Fig. 6. **First and second derivative of ψ with respect to F.** Quantities u_i and v_i are columns of U and V, respectively.

From Equation 5, we derive

$$\frac{\partial F_k}{\partial u_i}^T = \frac{\partial F_k}{\partial u_i(r, \phi, z)} \frac{\partial(r, \phi, z)}{\partial(x, y, z)}$$

$$= \begin{bmatrix} \frac{\partial \phi_i}{\partial r} & 0 & \frac{\partial \phi_i}{\partial z} & 0 & \frac{\phi_i}{r_k} & 0 & 0 & 0 & 0 \\ 0 & 0 & 0 & 0 & 0 & 0 & 0 & 0 & 0 \\ 0 & 0 & 0 & 0 & 0 & 0 & \frac{\partial \phi_i}{\partial r} & 0 & \frac{\partial \phi_i}{\partial z} \end{bmatrix} \left(\frac{\partial(x, y, z)}{\partial(r, \phi, z)} \right)^{-1}. \tag{7}$$

The tangent stiffness matrix is

$$K = \frac{\partial^2 \mathcal{E}}{\partial u^2} = 2\pi \sum_k \omega_k r_k \frac{\partial^2 \Psi}{\partial u^2} = 2\pi \sum_k \omega_k r_k \left(\frac{\partial F_k}{\partial u} \right)^T \frac{\partial^2 \Psi}{\partial F^2}_{|F=F_k} \frac{\partial F_k}{\partial u}. \tag{8}$$

4.4 Contact

We poke the object in a normal direction, and assume that friction is sufficiently large to prevent the elastic material under the circular contact to undergo a tangential sliding deformation during such poking. This assumption is reasonable because our specimens (silicon, foam, human tissue, rigid plastic) are dry non-slippery objects and we additionally apply magnesium climbing chalk powder to increase friction. Contact between the rigid cylinder and the elastic material is conforming; it forms due to our deep indentations to excite material nonlinearities. Therefore, if we know the indentation, we know the positions of all the contact vertices. We divide all mesh vertices into three groups: free vertices F, contact vertices C, and attached vertices A; the corresponding vertex displacements are denoted by u_F, u_C, u_A. The contact vertices are in contact with the rigid cylinder, and the attached vertices are fixing the elastic object to the ground at the bottom of the layer. Since u^C is known, we can solve for u^F using constrained optimization that minimizes the total elastic energy

$$\min_{u^F} \mathcal{E}(u^F, u^C, u^A). \tag{9}$$

The gradient and Hessian of the elastic energy have been derived above. We use Newton-Raphson iteration with a line search to solve the optimization problem. After u^F is computed, we can compute the total simulated contact force f^S as the sum of contact forces on all the vertices in C. We note that this sum equals the area integral of the normal pressure (i.e., no area-weighting is needed). This is because in FEM, discrete vertex forces already are area-weighted, even if mesh is non-uniform. The goal of our material optimization will then be for f^S to match the experimentally measured total contact force. We note that matching the contact force distribution

is not feasible because the distribution is not known (only the total force is measured), but our experiments (Figure 11) demonstrate that we can still recover the material.

5 NUMERICALLY STABLE STRETCH-BASED MATERIALS

In order to evaluate Equations 6 and 8, we need to be able to robustly evaluate $\partial \Psi / \partial F$ and $\partial^2 \Psi / \partial F^2$ for an arbitrary 3×3 deformation gradient F. We note that for isotropic elastic materials, there are two high-level approaches for modeling the elastic energy density Ψ: the invariant-based approach [Smith et al. 2019; Teran et al. 2005] and stretch-based approach [Xu et al. 2015]. The invariant-based approach models Ψ as a function of *invariants*, which are low-order polynomials of λ_i. We first attempted to model our experimentally fitted Ψ using invariants, but it was difficult to set a meaningful range for the invariants and adequately sample the invariants' 3D space; we were not able to reliably produce isotropic materials that match our real-world force/indentation curves using this approach. For example, the rest values of lower invariants i_1, i_2, i_3 [Smith et al. 2019] are 3, 3 and 1, respectively, and so on what intervals should they be sampled? Should the sampling region be a box, or some curved shape? Instead, we use stretch-based materials, whereby Ψ is modeled directly as a symmetric function of λ_i. Stretch-based materials are intuitive in the sense that Ψ directly models how the elastic energy varies when the material undergoes stretching and compression; we were able to reliably produce isotropic materials that match both synthetic experiments and real-world data. Compared to invariant-based material modeling, stretch-based material "force" curves are in our experience more easily interpreted by a human. This is because f, g and h are response due to changing "length", "area" and "volume", respectively. Furthermore, stretch-based materials decouple into *separable* Valanis-Landel [Xu et al. 2015] functions f, g, h for many common materials (Appendix A). In contrast, many common materials are not separable in terms of lower invariants i, ii, iii, including STS, Hencky, StVK and Ogden material. And so one would need to sample 2D functions $f(i, ii)$, not 1D functions $f(i), g(ii), h(iii)$. Doing so is more difficult than our approach of modeling 1D Valanis-Landel functions f, g, h of stretch-based materials (Section 6).

All that said, stretch-based materials as presented in [Xu et al. 2015] suffer from an important numerical weakness: there are singularities in the $\partial \Psi / \partial F$ and $\partial^2 \Psi / \partial F^2$ formulas when two (or all three) principal stretches become equal. If left unaddressed, this introduces simulation and optimization instabilities (Figure 7). We therefore contribute a solution to the singularity problem: we derive stable formulas for $\partial \Psi / \partial F$ and $\partial^2 \Psi / \partial F^2$, rigorously mathematically prove that the formulas are independent of the (infinite) choice of the
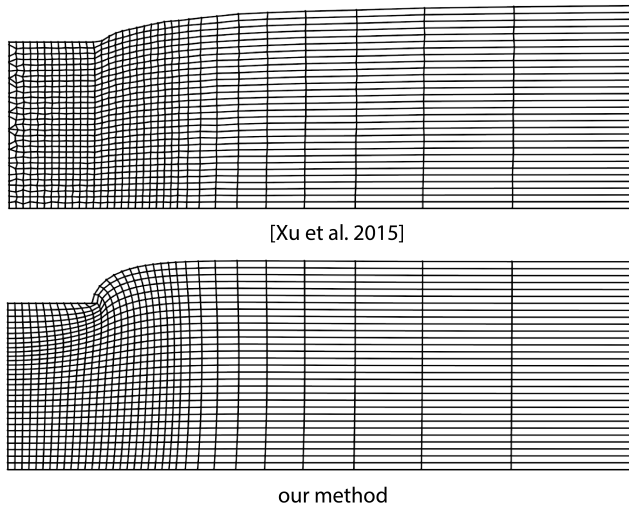
[Xu et al. 2015]

our method

Fig. 7. **Our singularity-handling stabilizes simulations of stretch-based isotropic materials.** Top: simulation produced using the stretch-based method of [Xu et al. 2015]. Bottom: our method numerically stabilizes stretch-based materials, by dealing with division-by-zero-inducing removable singularities, and projecting the elastic energy Hessian to be SPD.

SVD singular factors U and V, and give a method to project our Hessian $\partial^2 \Psi / \partial F^2$ to be SPD. We demonstrate that the Hessian takes on a very elegant block-diagonal form, paralleling those observed for invariant-based materials [Smith et al. 2019; Teran et al. 2005]. Figure 6 gives our final result; and the proofs are in Appendix C and Appendix D. We note that these results are independent of our material optimization focus, and apply generally to 3D stretch-based material simulation; but our motivation to use stretch-based materials stems from real-world material optimization. We would like to carefully delineate our contribution in relation to previous work. The existence of the block-diagonal form of the Hessian of isotropic functions has been known for a long-time [J.M.Ball 1984], and our basis in which the Hessian block-diagonalizes is the same as that for invariant-based materials in [Smith et al. 2019]. Recently, Zhu [Zhu 2021] also observed the Hessian block-diagonalization, and used it for 3D geometric shape modeling using stretch-based materials. However, the basis was expressed as a product of matrices and not given directly as in [Smith et al. 2019]. No prior work has stated the energy Hessian and its basis in such a clean and complete manner, or given mathematical proofs that, for stretch-based materials, $\partial \Psi / \partial F$ and $\partial^2 \Psi / \partial F^2$ are invariant to the choice of U and V in the presence of equal principal stretches; or given a strategy for how to numerically address the singularities; or projected the resulting Hessian to SPD. We contribute all of those important components (Appendix C and Appendix D).

6 GENERALIZED NEO-HOOKEAN MATERIAL

Stretch-based materials are convenient for material optimization because they directly model ψ as a function of material principal stretches λ_i, which is intuitive to understand and permits one to focus the analysis to certain practically relevant intervals $\lambda_{\min} \leq$

$\lambda \leq \lambda_{\max}$ with $\lambda_{\min} < 1 < \lambda_{\max}$. We note that computer animation research often analyzed cases where material inverts [Irving et al. 2004]. In our work, we analyze real materials, where the span of λs is more "modest", typically in the $0.5 - 1.5$ range. That said, our fitted materials are stable even outside of this range, and even under inversions (Figure 9), making them suitable for computer animation applications. The key challenge of modeling general isotropic materials is that the space of isotropic functions $\psi(\lambda_1, \lambda_2, \lambda_3)$ is infinite-dimensional and not easily parameterized. The most general parameterization that we are aware of, which still only expresses a strict subset of all isotropic functions, is the general Valanis-Landel family proposed in [Xu et al. 2015],

$$\begin{aligned}
\Psi = f(\lambda_1) + f(\lambda_2) + f(\lambda_3) + g(\lambda_1 \lambda_2) \\
+ g(\lambda_2 \lambda_3) + g(\lambda_3 \lambda_1) + h(\lambda_1 \lambda_2 \lambda_3),
\end{aligned} \tag{10}$$

where f, g, h are univariate functions. Note that this family is still infinite-dimensional because the space of univariate functions is infinite-dimensional. The rationale behind Valanis-Landel materials is that functions f, g, h model the elastic energy due to changing the length (of an infinitesimally small cube of material), surface area, and volume, respectively. Modeling isotropic spaces broader than Equation 10 is very hard because nobody has proposed any approach or equation for how such a broader space may be mathematically tackled. We initially attempted to model our materials using Equation 10, whereby we modeled f, g, h using univariate splines [Xu et al. 2015]. However, the resulting optimization was too indeterminate and did not consistently converge to the same f, g, h functions when presented the same force/indentation data. Therefore, we abandoned the f, g, h family and narrowed it to the family whereby f is modeled using a spline, $g = 0$ and h is modeled as a quadratic function of the log of the volume. We note that h could alternatively be modeled as a quadratic function of the volume (without the log) without any particular difficulty, but the presence of log is convenient because it allows our family to contain several well-known material families (below). This particular choice of modeling f, g, h is motivated by the fact that h is a volume-preservation term, and so it is natural to treat it separately; f generalizes a well-known material family (Neo-Hookean); and if g is not zero, it interferes with volume preservation under small deformations.

We note that all engineering applications of fitting stretch-based materials to date made the same $g = 0$ assumption, and actually, they made an even stricter assumption that the material is incompressible [Sussman and Bathe 2009; Valanis and Landel 1967], which meant that only f was modeled. We aim to model both compressible (foam) and nearly-incompressible (silicone, human tissue) materials. Our material family is richer than in the above references because we permit volume compressibility, controlled by our function h, in addition to f. Every nonlinear isotropic material has a linearization around the rest-shape; the space of such linearizations is two-dimensional, and can be parameterized with familiar Lamé parameters $\lambda_{\text{Lamé}}, \mu_{\text{Lamé}}$. These parameters, as well as familiar quantities such as Young's modulus and Poisson's ratio, can be easily
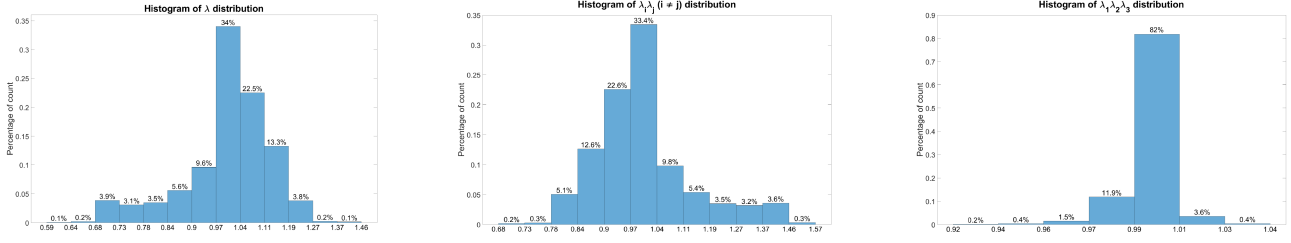
Fig. 8. **Distribution of the λ values:** Left: histogram of $\{\lambda_1, \lambda_2, \lambda_3\}$ values. Middle: histogram of $\{\lambda_1\lambda_2, \lambda_2\lambda_3, \lambda_3\lambda_1\}$ values. Right: histogram of $\{\lambda_1\lambda_2\lambda_3\}$ values. All λ values were computed using our FEM simulation, for a representative material.
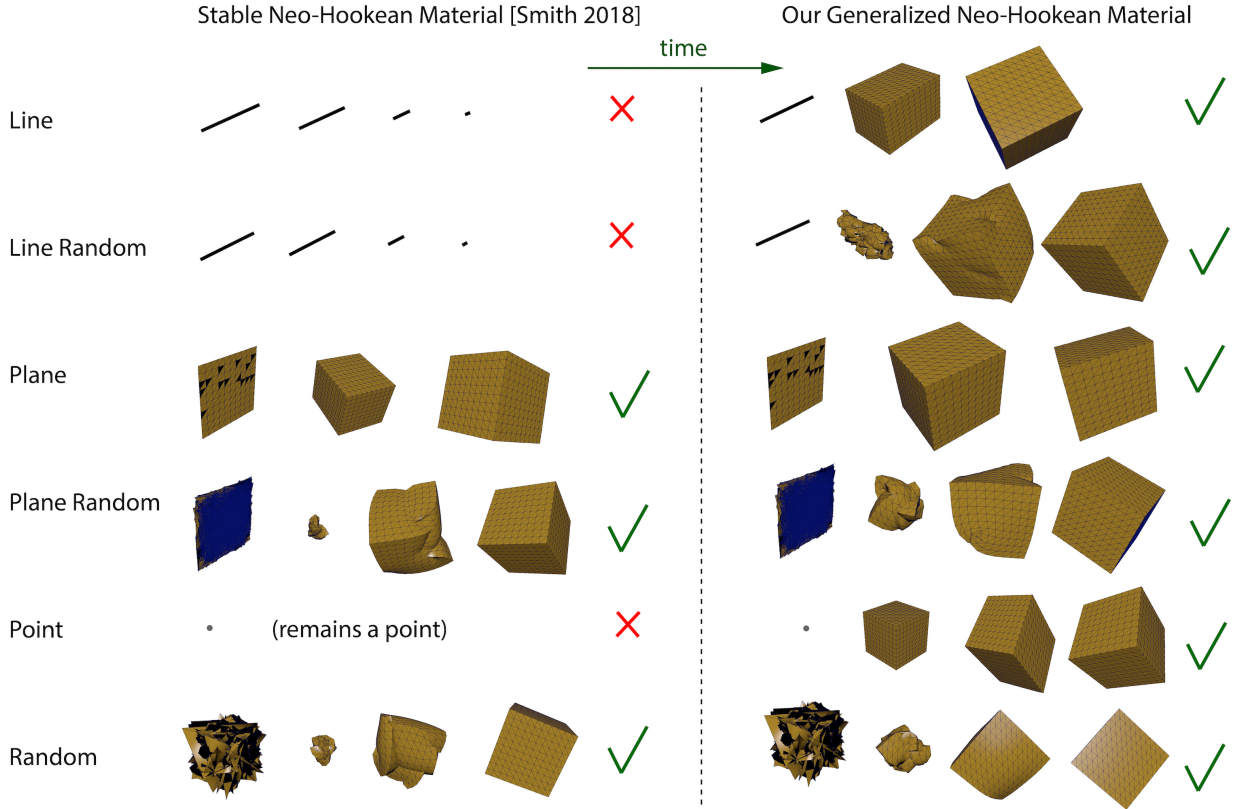

Fig. 9. **Test of stability of materials.** We subject the "Stable Neo-Hookean" (SNH) [Smith et al. 2018] material and our generalized Neo-Hookean to six stability tests. In "line", the cube is projected to a line. In "line random", the vertices are further randomized after the projection; this is a more difficult test. Analogous for "plane". Our material recovers in all cases, whereas SNH has difficulties when the geometry has collapsed to a point or to a line.

calculated from our parameters as follows

$$\mu_{\text{Lamé}} = \frac{1}{2}f''(1), \qquad \lambda_{\text{Lamé}} \text{ is a direct parameter}, \qquad (11)$$

$$E = \frac{\mu_{\text{Lamé}}(3\lambda_{\text{Lamé}} + 2\mu_{\text{Lamé}})}{\lambda_{\text{Lamé}} + \mu_{\text{Lamé}}}, \quad \nu = \frac{\lambda_{\text{Lamé}}}{2(\lambda_{\text{Lamé}} + \mu_{\text{Lamé}})}. \qquad (12)$$

After some trial and error, we determined that it is advantageous to model f as a natural cubic spline. In a typical natural cubic spline, one has $f'' = 0$ for very small and large arguments, which leads to indefinite Hessians and simulation instabilities. In order to model

stable energies f that grow quadratically for small and large values of λ, we instead set $f'' = C_{\text{small}}$ and $f'' = C_{\text{large}}$, for very small and very large λ, respectively (where $C_{\text{small}} > 0$ and $C_{\text{large}} > 0$ are subject to our optimization). Note that adding a constant to f only adds a constant offset to Ψ, and therefore we can set $f(1) = 0$ without a loss of generality. We set $f'(1) = 0$, which imposes that the material is in elastic equilibrium when all λ_i equal 1, i.e., rest shape. This is because for a general Valanis-Landel material, the equilibrium condition is $f'(1) + 2g'(1) + h'(1) = 0$, and the latter two terms are zero in our material family. The choice of natural

cubic splines for f means that f'' are piecewise-linear functions. We model these piecewise-linear functions using a set of control points (x_k, y_k), where $x_1 < x_2 < \ldots x_n$. We model our compressible materials as $h = 0.5\lambda_{\text{Lamé}}\log^2(\lambda_1\lambda_2\lambda_3)$, where $\lambda_{\text{Lamé}}$ plays the same role as the familiar "lambda" Lamé parameter.

For f, stability of our material can be enforced by requiring $f'' > 0$ [Xu et al. 2015]. For h, note that the above expression includes a log term, which is in principle unstable when $x \to 0$ [Smith et al. 2018]. However, we achieve stability by replacing h with a function h_{spline} modeled using our cubic splines that avoid the singularity in the log when the volume collapses to zero. This is done by evaluating $(d^2/dx^2)0.5\lambda_{\text{Lamé}}\log^2(x)$ at several (~ 20) logarithmically uniformly distributed samples on the $[1/e, e]$ interval, and setting those values as control nodes for our natural cubic spline h_{spline}, i.e., those values represent $(d^2/dx^2)h_{\text{spline}}$. In this manner, h_{spline} closely matches h on $[1/e, e]$, and extrapolates quadratically outside of this interval. Thus, we can achieve the favorable log behavior in the typical small/moderate deformation regime, and avoid the log singularity when the material collapses or inverts. Observe that this construction preserves the favorable property that the material is a linear function of $\lambda_{\text{Lamé}}$; this is because the control node values of h_{spline} are linear in $\lambda_{\text{Lamé}}$.

Our family includes several well-known materials that have been demonstrated suitable for modeling rubber-like materials, including the Neo-Hookean material, Hencky's material [Neff et al. 2016], STS material [Pai et al. 2018] and the Ogden material [Ogden 1972]. Of these families, all are parameterized with at most 3 parameters (lacking degrees of freedom to express complex material behavior), except Ogden which, like our family, permits an arbitrary large number of parameters. However, the key difference between our family and Ogden is that we can trivially express the stability condition $f'' > 0$ because the values of f'' are given by the control nodes of our natural cubic spline. In contrast, the same condition expressed for Ogden materials amounts to imposing that a univariate high-order polynomial, based on its coefficients, is strictly positive for all $x \geq 0$; this condition is mathematically very difficult/impossible to enforce in practice.

We note that there are many existing methods to capture material properties under small (linear) deformations, but we aim to capture the nonlinear behavior in f. We observe that even under relatively shallow poking (20% of the total sample depth), the deformation is large enough that the material behaves very non-linearly. Figure 8 shows the distribution of the principle stretches λ (computed using our simulation), when the poking depth is 20% of the total sample depth. Due to deformation effects at the cylinder boundary and due to volume preservation, this produces principal stretches as small as 0.55 and as large 1.5. This experiment establishes the range of λ where it is meaningful to fit our Ψ function, as Ψ cannot be determined for values of λ that do not appear in the actual deformed object. It also establishes that poking, despite being uni-directional, substantially excites not just individual values of λ, but also the product of all three λs, providing data to fit both f and h. In our work, a typical λ_{min} is ~ 0.5 and a typical λ_{max} is ~ 1.5 (Figure 8). By optimizing y_k, we can control the spline and the material. Similarly, the x_k are sampled log-uniformly in the range observed in Figure 8.
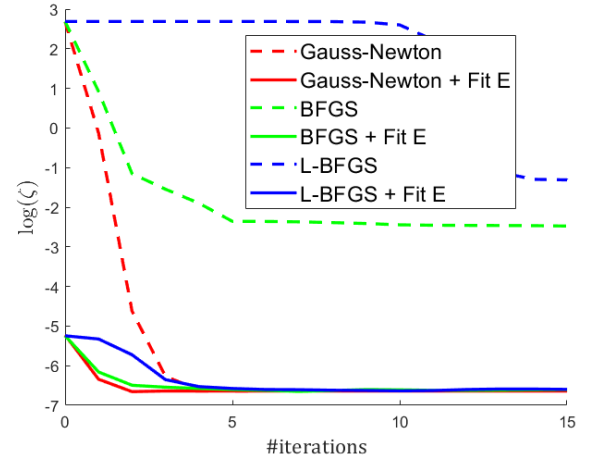

Fig. 10. **Convergence comparison:** We compare our Gauss-Newton optimizer to BFGS and L-BFGS, with and without our "Fit E" strategy. It can be seen that "Fit E" substantially accelerates convergence, and that the Gauss-Newton optimizer has the fastest convergence on our problem.

In particular, we use $x_k = e^{(k-(n+1)/2)\Delta s}$, for $k = 1, \ldots, n$, where n is an odd integer, and Δs is some suitable step size; in our work, it takes values 0.05, 0.1 or 0.2. Note that for $k = (n+1)/2$, we obtain $x_k = 1$, i.e., the rest shape is always a sample. Half of the remaining samples is less than 1 (compression) and half is more than one (extension).

In Figure 9, we systematically compare our material to an established industry "Stable Neo-Hookean" (SNH) material [Smith et al. 2018]. Both materials can recover from severely scrambled initial states. That said, unlike SNH, our material can recover even when the object is flattened to a line or to a point (see Figure 9). In this case, two (or three) principal stretches are zero. In the SNH material, when two principal stretches are zero, the material is pulled to a point, at which point all principal stretches are zero and the elastic force vanishes. There is no such stationary point in our material; it continues restoring the shape. As such, our material can be considered "animation-ready" and suitable for general-purpose soft body use in computer animation.

7 OPTIMIZATION

The goal of our optimization is to find the values $y_k = f''(x_k)$, and $\lambda_{\text{Lamé}}$ for h (collected into a material vector μ), so that the differences between the simulated contact forces and the captured contact forces are minimized. We measure the deviation of the simulated forces f_i^S from the experimentally measured contact forces f_i^E as

$$\zeta(\mu) = \sum_i ||f_i^S(\mu, u_i^F(\mu)) - f_i^E||_2^2, \qquad (13)$$

where i runs over all the poking samples. The gradient and Hessian of ζ with respect to material parameters μ are (derivation is in

Appendix E)

$$\frac{d\zeta}{d\mu} = \sum_i 2\big(f_i^S - f_i^E\big)^T \Big(\frac{\partial f_i^S}{\partial \mu} + K_i^{CF}\frac{\partial u_i^F}{\partial \mu}\Big), \tag{14}$$

$$\frac{d^2\zeta}{d^2\mu} = 2\sum_i \left(\left(\frac{\partial f_i^S}{\partial \mu} + K_i^{CF}\frac{\partial u_i^F}{\partial \mu}\right)^T \left(\frac{\partial f_i^S}{\partial \mu} + K_i^{CF}\frac{\partial u_i^F}{\partial \mu}\right) + \right.$$
$$\left. + \Big(f_i^S - f_i^E\Big)\left(2\frac{\partial K_i^{CF}}{\partial \mu}\frac{\partial u_i^F}{\partial \mu} + K_i^{CF}\frac{\partial^2 u_i^F}{\partial \mu^2}\right)\right), \tag{15}$$

$$\frac{\partial u^F}{\partial \mu} = -\Big(K^{FF}\Big)^{-1}\frac{\partial f^F}{\partial \mu}, \tag{16}$$

$$\frac{\partial^2 u^F}{\partial \mu^2} = 2\Big(K^{FF}\Big)^{-1}\frac{\partial K^{FF}}{\partial \mu}\Big(K^{FF}\Big)^{-1}\frac{\partial f^F}{\partial \mu}. \tag{17}$$

We now define our loss function

$$\ell(\mu) = \zeta(\mu) + \frac{\beta}{2}\mu^T L\mu, \tag{18}$$

where the quadratic form in the last term penalizes non-smoothness of f'', and $\beta \geq 0$ controls the smoothness. The "Laplacian" matrix L is computed by numerically approximating $\int_{\lambda_{\min}}^{\lambda_{\max}} f''(x)^2 dx$, using the usual numerical approximations, i.e., numerical integration and the familiar second-order approximation of the second derivative, resulting in the quadratic form L. Note that $\lambda_{\text{Lamé}}$ does not participate in this smoothness term. We found that a small amount of smoothness ($\beta \approx 10^{-14}$) is needed when fitting real materials to prevent f'' from overfitting to data. This regularizes the solution to exclude infeasible materials whose material curves are noisy or have high "jerk" (Figure 15, bottom). We enforce our $f'' > 0$ stability condition by clamping f'' to a small value (we use 1Pa; note that the unit for f'' is the same as for Lamé constants and the Young's modulus (Pa)). The presence of the β term substantially helps here, as it generally enables one to avoid clamping altogether.

Because we can compute the first and second derivative of ℓ with respect to μ, we used Newton's method (with a line search) to perform the optimization for μ. We note that we initially tried avoiding the Hessian by using nonlinear conjugate gradient optimization [Press et al. 2007], but the optimization was converging more slowly or in some cases did not converge.

During our optimization, we exploit the following observation, which substantially accelerated convergence (Figure 10; cutting the number of required Newton iterations by $\sim 2\times$). If we scale the elastic energy by a scalar $\kappa > 0$, then the static equilibrium mesh shape under poking remains the same, but the contact forces multiply by κ. The effect of this operation on μ is that all entries of μ simply multiply by κ. After every iteration, we find the optimal scalar κ to minimize $\ell(\kappa\mu)$ where μ is treated as constant. This can be done very easily and quickly as $\ell(\kappa\mu)$ is a scalar quadratic function of κ; we then update μ to $\kappa\mu$. Equation 12 shows that multiplying all entries of μ with κ multiplies Young's modulus by κ. Therefore, this operation can be understood as adjusting the overall material stiffness (i.e., Young's modulus) to match the experimental data; and therefore we refer to it as "Fit E" in Figure 10. In Figure 10, we also compare our Gauss-Newton optimizer to optimizers used in previous work. It can be seen that our optimizer converges faster than

that BFGS used in [Clyde et al. 2017], even when neither is using the "Fit E" strategy. Our "Fit E" strategy is not used in prior work, and forms one of our contributions; it substantially accelerates optimization. Figure 10 demonstrates that methods that do not use the "Fit E" strategy [Miguel et al. 2016] have a slower convergence. Our "Fit E" strategy is possible in our work because our material function is linear in the material parameters; this also enables the Gauss-Newton method to be a better approximator to the optimization objective Hessian than BFGS (see Figure 10). This is another difference to the method of [Clyde et al. 2017] whereby their material model is not a linear function of the material parameters, rendering BFGS a better choice for their optimization.

A special case of the "Fit E" idea is very useful at the beginning of our optimization, as it establishes a robust initial guess for μ, by finding good linear material parameters E and ν (or equivalently, $\lambda_{\text{Lamé}}$ and $\mu_{\text{Lamé}}$) to match the poking indentations and contact forces. This is done by assuming that f'' is constant (i.e., $f(x) = 1/2f''(1)(x-1)^2$), and restricting our μ to only contain $f''(1)$ and $\lambda_{\text{Lamé}}$, i.e., use a two-dimensional material family. Then, Equations 11 and 12 express $(\lambda_{\text{Lamé}}, f''(1))$ in terms of (E, ν) and vice versa. For each ν, we can therefore compute the optimal E using the "Fit E" procedure, and therefore evaluate $\ell(\nu)$ at this optimal $E = E(\nu)$. This in turn enables us to perform 1D minimization on ν, i.e., we can use this procedure to discover linear material parameters E and ν. We then expand the optimization to the full μ, whereby these "pre-optimized" $f''(1)$ and $\lambda_{\text{Lamé}}$ serve as a good initial guess.

In order to test the robustness of our optimizer, we performed the following synthetic experiment. We generated several "random" materials μ, by modeling a "random" f'' and $\lambda_{\text{Lamé}}$ using 1D Perlin noise. For each such material, we then created synthetic poking forces/indentations by running our poking FEM simulation. We then discarded μ and performed optimization to re-discover μ, based on the poking forces/indentations. Our optimizer was successful in each of the five such random tests, i.e., robustly recovered the correct μ. A representative test is shown in Figure 11. We note that, as a consequence of re-discovering μ, our optimizer also recovered the correct linear material properties, i.e., Young's modulus and Poisson's ratio. The success of this experiment has three implications. (1) It is possible to estimate volume preservation by poking with multiple radii. (2) Our material model is robust against local minima. (3) Our optimizer is able to recover the material without knowing surface or volumetric displacement data, enabling our technique to work without vision sensors.

8 RESULTS AND VALIDATION

We measured the ψ function of three two man-made materials: foam ("Soma Foama 15"), silicone ("Dragon Skin FX Pro") and a chair cushion. We manufactured the foam and silicone materials using the chemical ingredients purchased at "SmoothOn Inc." [SmoothOn 2020]. We validated the optimized materials by poking them with shapes that were not used in the optimization, and then comparing the predicted simulated contact forces and the real measured contact forces. We also validated the optimized materials on a 3D mesh, poked with a rigid object with a square profile. Our validations also include a pulling test, as well as a durometer-based validation. We
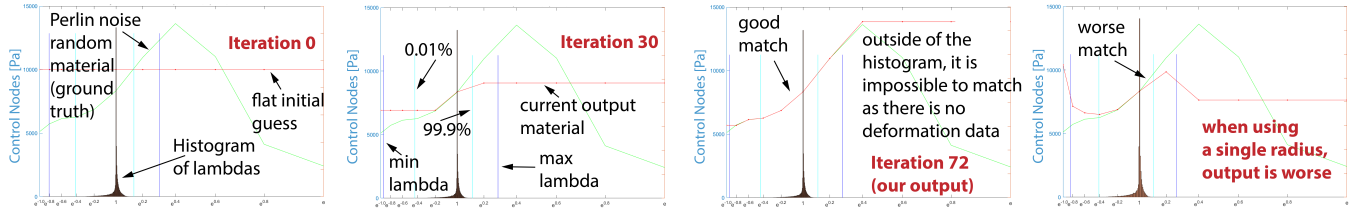
Fig. 11. **Test of robustness of our optimizer:** The optimizer re-discovers a material μ simply from the synthetic poking force/indentation data created from a FEM simulation using μ. The ground truth "generator" material μ and the re-discovered material are shown as green and red curves, respectively. Diagrams also show the histogram of λ values generated by a poking FEM simulation under the current material; dark blue lines show the minimum and maximum λ appearing anywhere in the simulation data, whereas light blue lines show the 99.9% and 0.01% percentiles. The optimizer cannot discover μ for principal stretches λ that are outside of the histogram, because there is no λ deformation data to base $f(\lambda)$ on. Initial guess is a constant material. At the end, our optimizer discovers μ everywhere where there is data for λ. RMS force error is decreased to a very small value, and the discovered Young's modulus 10357 Pa and Poisson's ratio 0.243 closely match the true values of 10356 Pa and 0.243. The left-most three images show the optimization that uses poking data under five cylinder radii. For comparison, the right-most image shows the optimization that uses a single radii (the match to ground truth is worse). This demonstrates that poking with multiple radii is advantageous as it better captures the material nonlinearity. Prior work [Pai et al. 2018] used a single radius.

Table 1. **Optimization performance:** Initial and final objective function ζ, number of optimizing iterations, and optimization time.

Material name	initial ζ	final ζ	#iter	time
Foam	0.011	0.002	10	17 mins
Silicone	0.181	0.038	14	34 mins
Chair cushion	0.202	0.002	54	73 mins
Human upper arm	$1.82 \cdot 10^{-4}$	$5.56 \cdot 10^{-7}$	10	5 mins

also show that our method can estimate the depth of the material layer, if it is unknown. All examples were computed on a 3.00 GHz Intel Xeon i7 CPU E5-2687W v4 processor with 48 cores. Table 1 shows the change of ζ (Equation 13) during our optimizations, and the time spent for optimization.
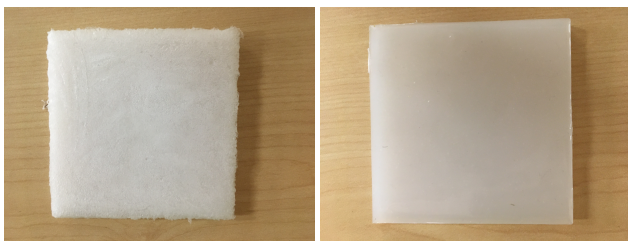

Fig. 12. **Man-made materials:** Left: foam ($\nu = 0.21$). Right: silicone ($\nu = 0.495$).

8.1 Silicone

We manufactured a 10cm x 10cm x 0.5cm silicone material layer using the "Dragon Skin FX Pro" silicone material [SmoothOn 2020] (Figure 12, right). We used two cylinder radii to fit Ψ, whereas the other radii were used for validation only. Figure 14 indicates that our fitted material approximates the captured forces well, under different contact area sizes. In Figure 15, we give f'' for the optimized silicone material. The value of $\sqrt{\zeta}$ was reduced by 89%, from 2.192 to 0.237. Figure 15 also gives an example failure case when
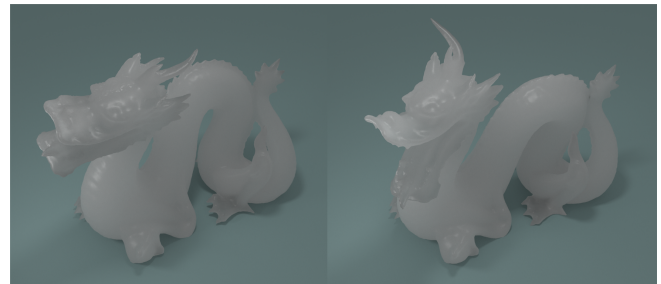

Fig. 13. **Silicone dragon simulated using our acquired material.** The dragon is sized to be 10m in length. Rayleigh stiffness damping (0.002).

not using optimization regularization (i.e., $\beta = 0$). Figure 13 shows a FEM simulation of a dragon using the fitted silicone material.

8.2 Foam

We manufactured a 10cm x 10cm x 1cm foam material layer using the "Soma Foama 15" foam material [SmoothOn 2020] (Figure 12, left). Foam is softer than the silicone discussed above and has a lower Poisson's ratio. We poked the foam with cylinders with radii of 1.03mm, 2.06mm, 3.01mm, 4.05mm and 5.06mm, and used this data to fit the material (Figure 17). The value of $\sqrt{\zeta}$ was reduced by 58%, from 0.104 to 0.044. In Figure 16, we simulated a turtle model (courtesy of [Barbič et al. 2012]) using our optimized material, and compared it to the best Neo-Hookean material optimized to the same data (also seen in Figure 17). Our method makes it possible to transfer materials acquired from real objects into plausible digital/virtual computer animations of such materials.

8.3 Chair Cushion

We used our portable laser device to measure the material of a chair cushion (Figure 3, c). Our generalized Neo-Hookean material is capable of fitting the laser measurements to a good extent (Figure 18).
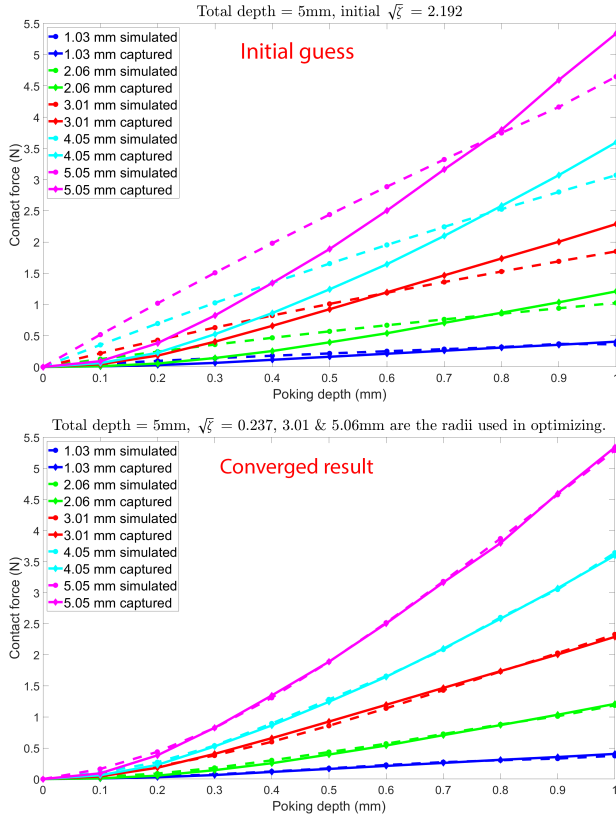
Fig. 14. **Fitting and validation for the Dragon Skin FX Pro silicone material:** We used the cylinders with 3.01mm and 5.06mm radii to fit Ψ. Top: the captured and simulated force-indentation curves for the **initial guess** material. Bottom: the force-indentation curves for the optimized material. The optimized material is shown in Figure 15.

8.4 Human upper arm

In this experiment, we measured the nonlinear material of a human upper arm, using our laser and force meter. We first used ultrasound to measure the distance from the skin to the humerus bone (3cm), and then poked the skin with our untethered laser setup (Figure 19). We note that this experiment makes several simplifying assumptions: the upper arm is not an infinite object and has curvature; the material in the arm is not locally homogeneous in the normal direction (but is reasonably tangentially homogeneous), because there are at least two layers with significant depth (subcutaneous fat and muscle), in addition to the dermis and epidermis. We provide a systematic analysis on the effect of such simplifications to the measured material properties in Figures 20, 21, 22. Despite the simplifying assumptions, our model qualitatively captures the relationship between real indentations and forces (e.g., it reports a Young's modulus consistent with the generally accepted values for human fat, which are in the 1000-3000 Pa range). Our model is an example of a phenomenological model (see [Pai et al. 2018] for an excellent exposition on this topic). In science and technology, various models are often applied outside of their initial range of validity.
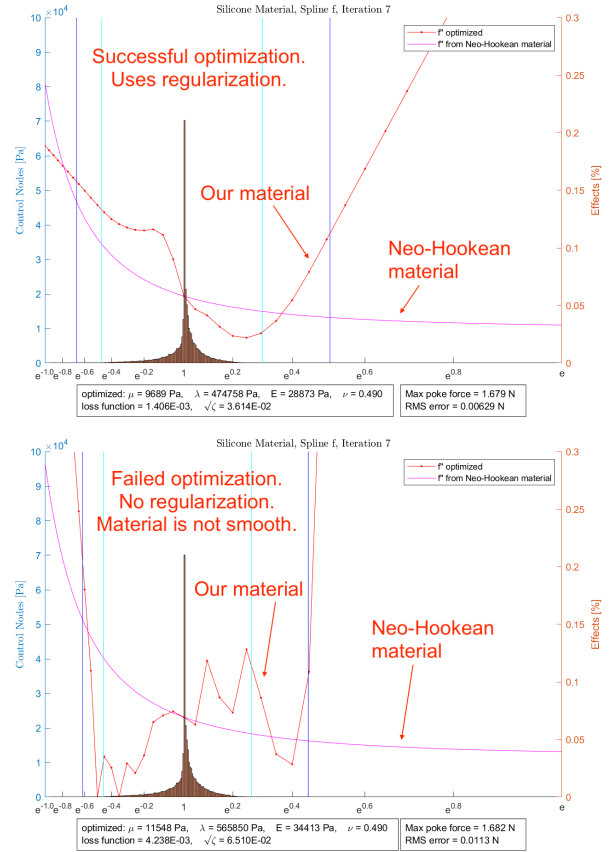
Fig. 15. **Dragon Skin FX Pro silicone material curves.** Top: the successfully optimized silicone material, using regularization $\beta = 10^{-15}$. Bottom: failed material optimization when not using regularization ($\beta = 0$).
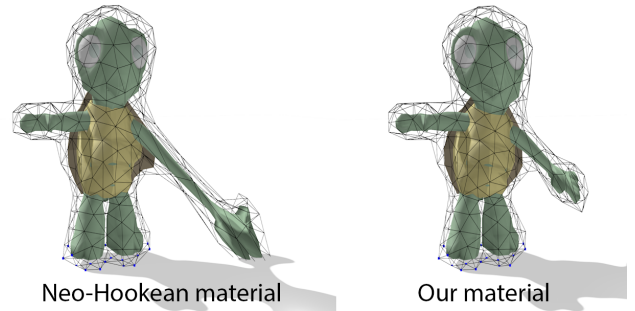
Fig. 16. **Our fitted material vs fitted Neo-Hookean material:** We use the same poking data to fit both materials. Neo-Hookean material is too soft under large deformations, whereas our material stiffens under large deformations, similar to real foam.

Even though "incorrect", the models are still useful, especially when more precise models are not available. For humans, our method subsumes the different layers (fat, muscle, etc.) with a single model, which could be useful for modeling contact between the external
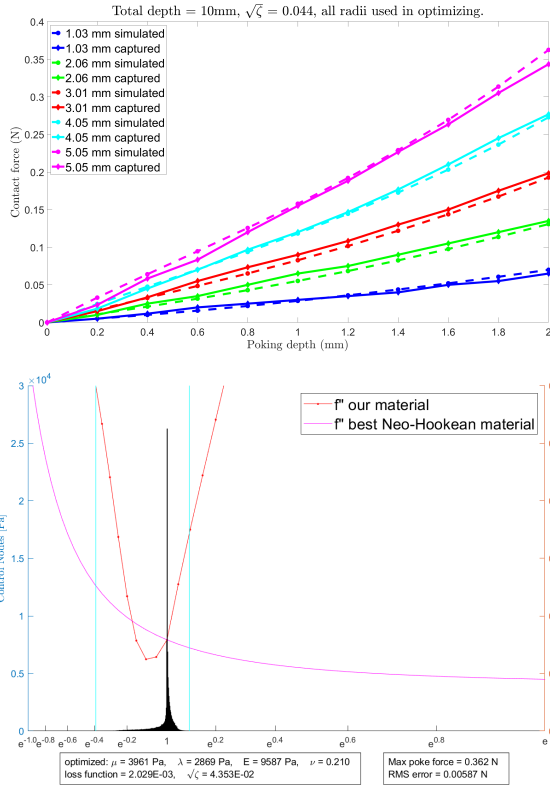
Fig. 17. **Fitting of the Soma Foama 15 material:** We used five cylinder radii to fit Ψ. Top: the captured and optimized force-indentation curves. Bottom: our optimized material ($\sqrt{\zeta} = 0.044$). Also shown is the best optimized Neo-Hookean material, which is substantially different to ours and has a worse score ($\sqrt{\zeta} = 0.076$).

Fig. 18. **Measuring the material of a chair cushion:** We obtained the force-indentation relations on a chair cushion with our portable laser device and then fitted our material. The simulated forces match the measured ones well. The radius of 3.01mm was used for the training data; the other radii are used for testing.

objects and the human skin. This experiment was performed under a proper IRB permission of our institution.
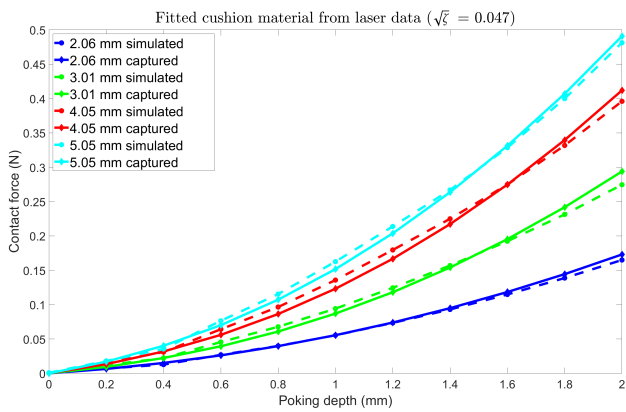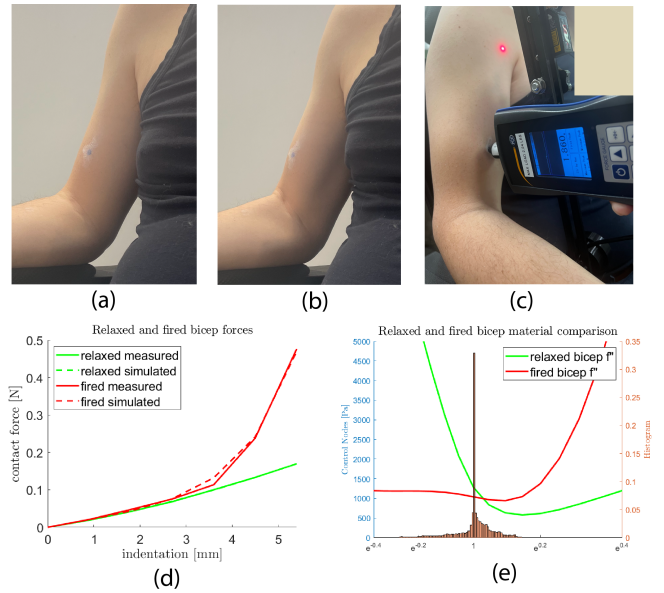

Fig. 19. **Measuring the material of the human arm:** We used our laser and force meter to capture the forces and indentations on a human upper arm (c). We did so twice, once with a relaxed bicep (a), and then with a fired bicep (b). Note that this particular spot on the arm is quite soft, with a substantial subcutaneous fat above the muscle. Image (d) shows the experimentally measured forces and indentations ($r = 3.01mm$) as well as their simulated counterparts obtained with the fitted materials; note that the relaxed measured and simulated curves are on top of each other. Image (e) shows the fitted materials for the relaxed and fired bicep. In this example, we used a known Poissons' ratio $\nu = 0.49$, which is a value cited in medical literature [Payne et al. 2015] for human muscles, and therefore we poked with just one radius. As can be seen in (d), under small displacements, the relaxed and fired biceps have similar stiffness; this is because for small displacements, the plastic cylinder is still primarily pushing into the subcutaneous fat. Consequently, the measured relaxed and fired Young's modulus were relatively similar, namely 1908 Pa and 2190 Pa, respectively. Eventually, under a deeper poke, muscle starts participating more in the contact stiffens in the case of the fired muscle. As expected, it can be seen in (e) that the fired bicep material is generally stiffer under large deformations, but both materials are similar at around $x = 1$, i.e., for small deformations; this is consistent with (d). Note that while f'' reaches 0 in this example for large lambdas, i.e., tensile stiffens becomes progressively weaker under large stretches, the material also has the volume-preserving h term to remain stable.

8.5 Validation of orthogonality, planarity and homogeneity

In our paper, we assume that the poking indenter is orthogonal to the investigated elastic surface. We also assume that when undeformed, the elastic surface is planar, and that it has homogeneous material properties in the vicinity of contact. In practice, it is not possible to ensure that these properties are perfectly satisfied. In this subsection,
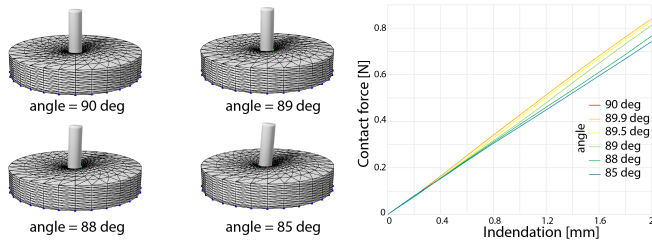
Fig. 20. **Error in forces when the indenter is not orthogonal to the elastic surface.** The contact force vs indentation curves were obtained via 3D FEM simulation (i.e., not using our 2D technique, as in this experiment the setting is not radially symmetric).
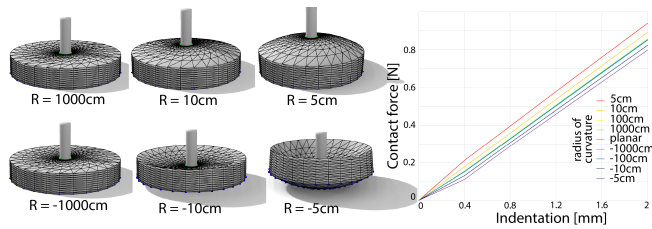

Fig. 21. **Error in forces when the elastic surface is not planar.** The contact force vs indentation curves were obtained via 3D FEM simulation.
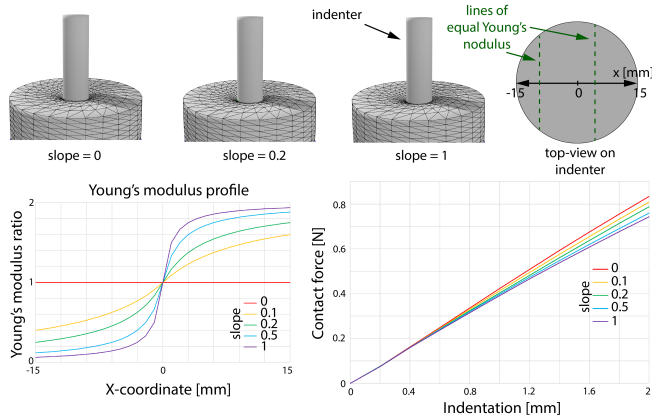

Fig. 22. **Error in forces when the elastic material is not locally homogeneous.** The contact force vs indentation curves were obtained via 3D FEM simulation. The poking radius (radius of indenter) is 3mm, and the radius of the poked elastic cylinder is 15mm. We vary the Young's modulus in the x-direction; Young's modulus is constant in y and z (top-right subfigure). The "Young's modulus profile" subfigure shows how the Young's modulus varies in x (we use the sigmoid function); the "slope" is the curve slope at $x = 0$ and the "Young's modulus ratio" refers to the ratio between the Young's modulus at x and that at $x = 0$. Higher slopes produce a more drastically varying local Young's modulus distribution. Such a sigmoid gradient profile of Young's modulus was selected so that we never generate zero values of Young's modulus, and so that there is substantial variability in the Young's modulus; we first tried linear profiles, but those were not sufficiently variable, producing even smaller relative contact force errors.

we quantitatively analyze the error in optimized materials if these assumptions are violated.

Figure 20 analyzes the error in optimized materials when the poking angle deviates from 90 degrees. Even at an angle of 85 degrees and when poking the material at 2mm (20% of the total material depth of 10mm, i.e., very nonlinear poking), the maximum relative error in the contact force is approximately 10%, which would cause the same error in the measured Young's modulus. Observe that an angle of 85 degrees is clearly visible to the human eye (Figure 20), and therefore can be guarded against during the untethered poking with our laser device. The error is smaller at angles closer to 90 degrees. When using the force stand, the angle can be made much more precise by adjusting the force meter housing screws, easily down to 1 degree or better, at which point the error is under 3%. Such errors are reasonable given the imperfection of measuring equipment, especially given the simplicity of our setup. In computer graphics applications, one usually does not need exact materials, but needs reasonably accurate materials that qualitatively reproduce the elastic behavior (Figure 27).

Figure 21 analyzes the error in optimized materials when the elastic surface is not planar, but is instead the surface of a sphere, under several radii. Even when the sphere radius is very small (5cm; comparable to curvatures in the human body), the relative error in the contact force and estimated Young's modulus is still only about 10%. Note that state-of-the-art prior work [Pai et al. 2018] also simulated the human body as locally flat, in their case as elastic cylinders of a finite radius.

Figure 22 analyzes the error in optimized materials when the investigated elastic material is not homogeneous, but instead its Young's modulus varies as a gradient from one side of the poked cylindrical elastic object to the other side. Largest relative error in the contact force and estimated Young's modulus is 9%, for a very drastically changing Young's modulus distribution across the elastic specimen.

8.6 Validation via pulling

The materials in this paper are determined based on poking the object. Perhaps counter-intuitively, during poking, material undergoes both compression and stretching. Therefore, while poking causes more compression than stretching, both are substantially present in the poking data (see Figure 8; there are even stretches with $\lambda > 1.5$ present in the data). As shown in our experiment (Figure 11), such poking data, obtained under multiple poking radii, is sufficient to recover the material. Our setup therefore does not require displacement objectives or biaxial tests to recover material properties; this is one of our contributions. Still, we performed a validation on how well our materials that were fitted by poking perform under stretching (Figure 23). Our material matches the ground truth forces well, better than Neo-Hookean materials (Figure 23).

8.7 Validation with a durometer

We validated our materials against a standard durometer (Figure 24) of the "Shore 00" type; this type is suitable for measuring soft elastic objects such as silicone and the human skin. A durometer only
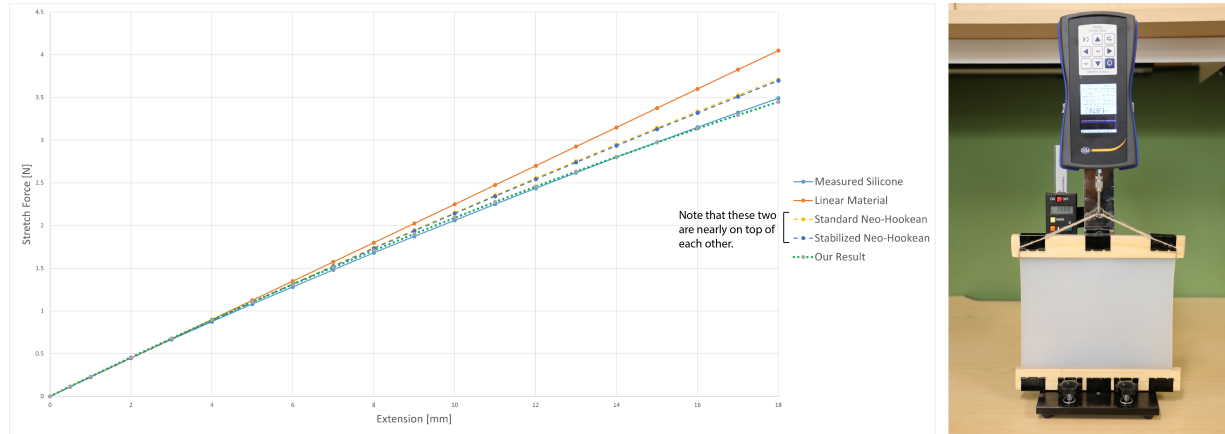
Fig. 23. **Validation via pulling.** We first used force vs indentations poking data (Figure 14) to fit the silicone nonlinear material, as described in Sections 3-7. Next, we measured real stretching forces ("Measured Silicone") using the setup shown on the right, similar to the one used in [Wang et al. 2011] to measure cloth material properties. We sandwiched the silicone slab in between wooden planks at top and bottom. At the bottom, the planks are fixed to the base of the force meter. By turning the wheel of the force stand, we stretched the silicone "slab" (15cm x 15cm x 1cm), and measured the total stretching force (via force meter) and the extension (via the force stand displacement display). We stretched the silicone by 12%, which is in the nonlinear region (see the linear curve for comparison). We incorporated gravity into the experiment by measuring the mass density of silicone. Finally, we ran FEM simulations under those fitted materials, comparing them to "Measured Silicone". Our material matches the "Measured Silicone" well, and more closely than the best Neo-Hookean materials.
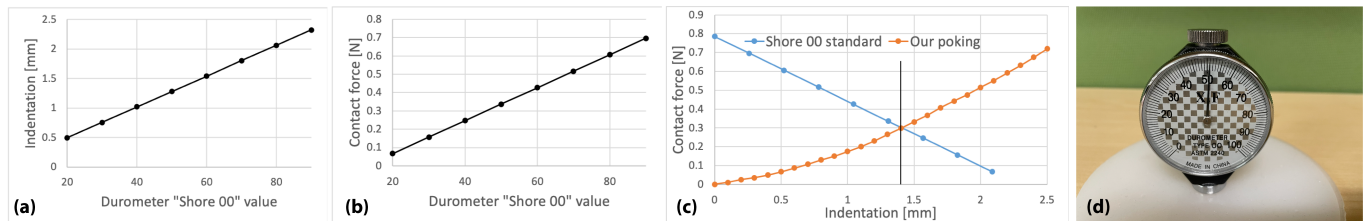

Fig. 24. **Validation with a durometer.** (a), (b): the "Shore 00" indentation and contact force from the durometer ASTM D2240-15 standard. (c): The indentation corresponding to the "Shore 00" value is the intersection of the two curves. (d): Real durometer value (51.0) is close to value predicted by our experiments (54.2).

measures a single indentation point that cannot be directly prescribed by the user, namely the one that places the durometer's pin in static equilibrium against the contact forces. There is a 1:1 mapping between the translation of the durometer pin away from its neutral position, the Shore 00 value and the force in the durometer. These relationships are standardized [International 2021], and are the same for all durometers of the same type (Figure 24, (a), (b)). The indentation equals the length of the exposed pin when not in contact (standardized to 2.5mm) minus the upwards translation of the pin. On the diagram where x-axis is indentation and y-axis is contact force, we plot the measured data from our poking, and the standardized durometer data (Figure 24, (c)). The intersection of these two curves gives the actual indentation, from which the "Shore 00" value can be recovered using the durometer standard (Figure 24, (a)). We performed such an experiment for the silicone, and measured "Shore 00" value to be 54.2. A real durometer measured 51.0 (Figure 24, (d)). The discrepancy, while small given that we are predicting real materials, occurs because it is difficult to place the real durometer's casing into the position of the exact onset of contact; this can easily introduce a 5-10% experimental error. We

found that real durometers, despite the standard, generally all suffer from this limitation.

8.8 Convergence under mesh refinement

To validate our 2D simulation, we compare the contact force computed using 2D simulation to 3D tetrahedral FEM simulation, under identical poking conditions. Figure 25 shows that as the number of mesh divisions increases, the 2D and 3D forces converge to the same value, validating our 2D simulation approach.

8.9 Extension: Estimating the depth of the material layer

In some applications, material depth is not known, and so we here demonstrate that our method can also be used to estimate the material depth. We do so by running optimizations under different depths, and then select the depth that produces the smallest converged ζ. Such an approach could be suitable, for example, for in-vivo human tissue measurements. In Figure 26 we ran such an experiment on the silicone material with a true depth of 5mm; with guesses for the depth ranging from 3mm to 9mm. The lowest ζ is achieved for 5mm;
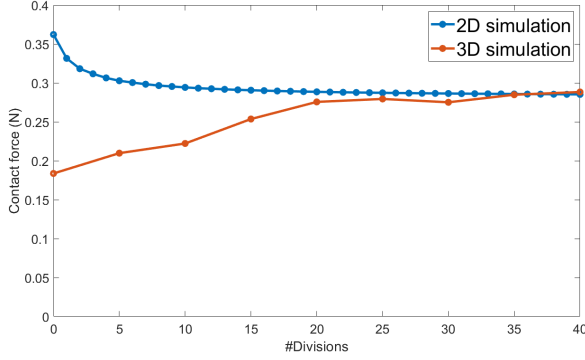
Fig. 25. **Validation of our 2D simulation method:** Contact forces computed using our 2D method converge to forces computed using a 3D method. "Divisions" is the mesh radial resolution under contact (see Figure 5).

i.e., the ground-truth value, validating that our method produces Ψ that matches the real-world material behavior.
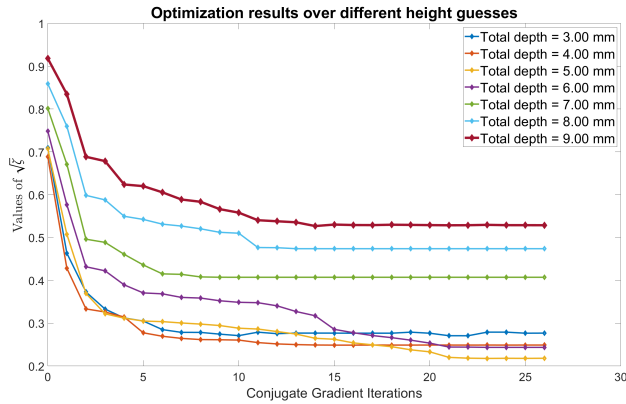

Fig. 26. **Discovering material depth through optimization:** We show how ζ decreases vs optimizing iterations, for several guesses of the depth. We successfully recover the ground truth (5mm) as the depth that produces the lowest converged ζ value (orange curve). Silicone material.

8.10 Validation against a real object of the same material

In Figure 27, we performed a validation whereby we measured a real object (both geometry and material properties), and then created a virtual replica, which we subject to identical squeezing as the real counterpart. We then compared the simulation result to the photograph, observing that our material + simulation produce a result that closely matches the photograph. In Figure 27, we also compared our best fitted material to [Smith et al. 2018], and demonstrated that our material is more stable and capable of matching the photographs, whereas [Smith et al. 2018] produces artefacts.

8.11 Validation via 3D simulation on a complex elastic shape

We also tested our fitted material in a challenging scenario where the object assumes a general 3D shape and the contact setup is not

axially symmetric. We first manufactured a thin layer of silicone material, and measured Ψ for it using our 2D simulation method and optimization. We then manufactured a silicone Stanford bunny from the same material. We then pushed a cube against the bunny, and measured the real contact force profile vs real indentation, using our force meter and force stand. We then built a digital twin of this setup, by employing 3D FEM simulation on a bunny 3D tetrahedral mesh that used our optimized Ψ material. The computed simulated forces are close to the captured forces (Figure 28), validating our material acquisition process. Note that the cube has a square profile, whereas the poking objects to determine the material were round, and therefore this provides an additional validation that our materials work correctly even if the indenting object has different geometry than during material capture.

8.12 Comparison to the STS material

In this section, we compare our generalized Neo-Hookean materials to the "STS material" used in [Pai et al. 2018] (formulas for STS are in Appendix A). Because our material family includes the STS material, we can reasonably expect for our optimizer to find a material that better fits the captured data than any STS material. To prove this, we need to compare them in a quantitative way. We optimized both our spline-based generalized Neo-Hookean material and the STS material against the Foam-15 force data at a poking radius of 3mm. Next, we test the resulting material on 3 radii (1mm, 3mm, 5mm), by comparing the simulated forces to the captured forces. Our material fits the captured forces better than the STS material, especially in the 5mm radius case (Figure 30). Note that the STS material contains the Neo-Hookean material as a special case, and therefore this "material ablation" study also establishes that our materials better fit experimental data than Neo-Hookean materials.

8.13 Performance speedup due to our mathematically equivalent 2D simulation

We also performed a timing comparison experiment. In [Pai et al. 2018], they optimize materials using a 3D mesh simulation, which is expected to be a lot slower than our mathematically equivalent 2D simulation. Indeed, our experiment confirms this. We procedurally generated our 2D simulation mesh at several subdivision levels. At each subdivision level, we then generated a corresponding hexahedral mesh by rotating the 2D simulation mesh 360° around the vertical axis, whereby the number of angular sectors was chosen so that the "angular" size of the resulting hex cells is approximately equal to the "radial" and "height" sizes. We then divided the hex cells into tets for simulation. In this manner, at each subdivision level, the precision of the 3D simulation is approximately equal to the precision of the 2D simulation, as they both employ the same discretization in the radial and height directions. Note that strictly speaking, at the same subdivision level in this experiment the 2D simulation precision is always higher because the angular integral is computed analytically vs approximated in sectors as in the 3D simulation. Therefore, this experiment is slightly unfair to our method (2D simulation); we neglect this effect here. We measured the computation time of one simulation timestep of the 2D and 3D FEM simulation. As expected, the 2D simulation takes much less time
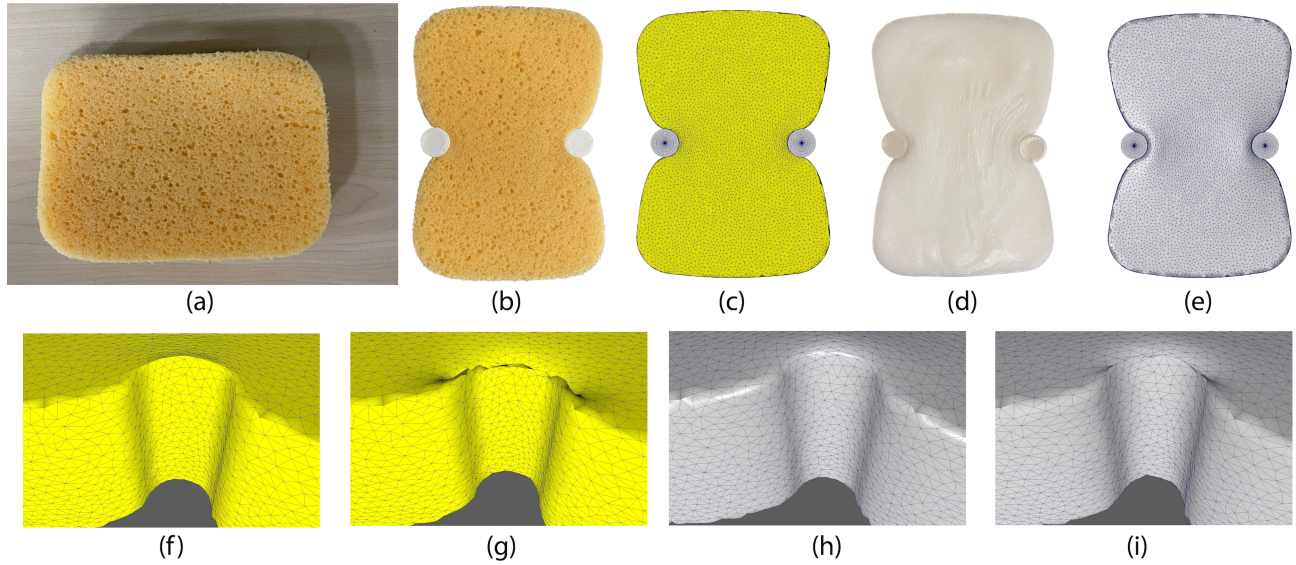
Fig. 27. **Validation against a real object made of the same material:** (a) We start with a familiar object (car sponge). We measure the sponge material using the poking techniques of our paper. Because the sponge has interior voids, one can readily observe in the real world that it does not preserve volume; we use Poisson's ratio of 0.0. (b) In the real world, we squeeze the sponge in between two vertical rigid cylinders and take a photo. (c) We simulate the sponge using our fitted material, squeezing it against the same vertical rigid cylinders. We observe that the shape closely matches (b). (d) We manufacture a foam sponge of the same shape, by creating a 3D-printed mold (not shown) and casting the foam into it; we measure the foam material using the poking techniques of our paper. We optimize $\nu = 0.21$ as the best fitting ν to the poking data. We squeeze the foam in the real world in the same manner as the sponge, and take a photo. (e) We simulate the foam using our fitted material, squeezing it against the same vertical rigid cylinders. We observe that the shape closely matches (d). (f,h) Detail of our simulation result on the sponge and foam (our optimized material), respectively. (g,i) The simulation result obtained by optimizing the stable Neo-Hookean material to the sponge and foam poking data [Smith et al. 2018], respectively. The material produces shape artefacts along the rim of the indentation; we tried several simulator/integrator settings and could not remove the artefacts.

Fig. 29. **Stanford bunny experiment:** We poke the bunny using a rigid object with a square profile. Two camera views are shown. Silicone material.

Fig. 28. **Validation using 3D simulation on the Stanford bunny:** The simulated contact forces computed using 3D FEM on a tetrahedral mesh, using the material optimized using our 2D method, closely match real contact forces under real indentations. Silicone material.

than the 3D simulation, and this difference grows larger with the number of subdivision levels (Figure 31). Note that simulation is the core computational operation performed inside each optimization iteration. In our experiments, the resolution level is typically set to 5

(i.e., the number of elements across the indenting cylinder's diameter is 10), at which point our 2D simulation is 30× faster than equally precise 3D simulation. Therefore, this difference in simulation speed is very significant for our optimization.

9 CONCLUSION

We proposed an isotropic material model that generalizes Neo-Hookean materials to be able to model nonlinear tensile stiffness. This is achieved by modeling the f function of a Valanis-Landel stretch-based material using splines. The resulting material can fit the hyper-elastic isotropic behavior of man-made materials such as foam and silicone, and can also serve as a phenomenological model
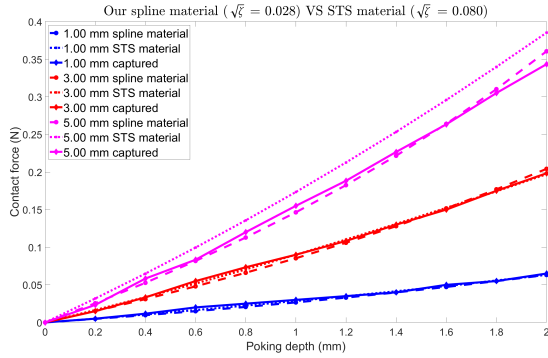
Fig. 30. **Comparison to STS material:** We used the foam-15 force/displacement data at a radius 3mm to fit both our spline-based generalized Neo-Hookean material, and the STS material. We then tested the resulting materials on other radii. Our material fits the captured force/displacement data better.
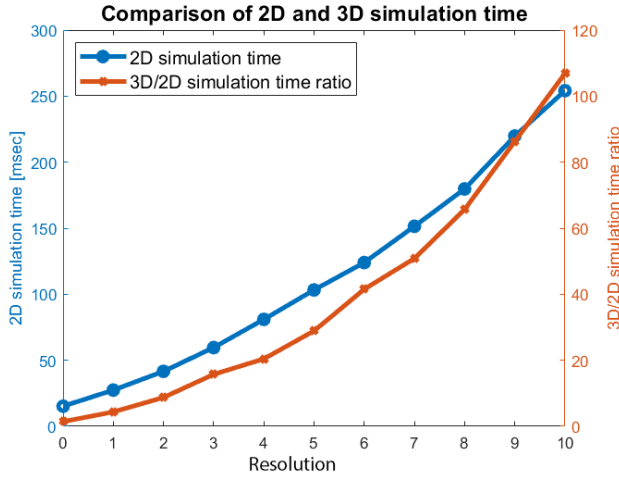
Fig. 31. **2D vs 3D simulation time:** We measured the time for one simulation step for our 2D simulation and compared it to a 3D simulation that uses the same mesh accuracy. The 2D simulation time scales much better as the resolution increases.

for human tissue. We also developed a systematic poking procedure to capture the force-indentation profile and an optimization method to fit the material properties. For large objects that cannot be put into a force stand, we propose an inexpensive laser-based instrument to simultaneously measure forces and indentations. We also substantially improve the numerics of general stretch-based isotropic materials, by creating a technique to deal with division-by-zero-induced removable singularities that previously impeded applications of stretch-based materials, and by analyzing the eigenvalues of the Hessian of the elastic energy and projecting it to SPD. We compare our generalized Neo-Hookean materials to state-of-the-art Neo-Hookean materials [Smith et al. 2018], and demonstrate improved stability of our materials; as such, our materials can also

be used for general-purpose soft-body simulation work in computer animation. We also demonstrate how to exploit the rotational symmetry of the poking problem to simplify the simulation to a mathematically identical 2D simulation, which accelerates the optimization 30 ×.

Accurate simulation that matches real objects is a key goal of physically based simulation. In order to benefit from our accurate materials, one needs a precise (offline) soft-body solver and a reasonably detailed mesh, which typically precludes direct real-time simulation. There are, however, techniques to accelerate such simulations for real-time applications, such as model reduction [Sifakis and Barbič 2012]. Furthermore, precise offline simulation can produce training data for machine learning, which can then be used to replicate the highly precise outputs in real-time [Bailey et al. 2020].

We extensively validated our method through various experiments, including 2D to 3D simulation comparisons, an ablation study where we fitted the experimental data using a less "powerful" material (STS), a validation against photographs of deformed real objects, a pulling validation, a validation with a durometer, poking a general 3D object (bunny) made of our acquired material, and comparing real forces to simulated forces. Our optimizer has been validated by generating a random synthetic material and then rediscovering this material based on the poking data generated from it in a simulation, and by comparing several optimization strategies (Gauss-Newton, BFGS and L-BFGS). Our material family includes several popular materials as special cases, but is significantly broader and can help explore new, unforeseen materials. In this perspective, we took a step towards understanding elastic materials with a lesser inductive bias. Our optimization process along with our acceleration techniques enable us to rapidly obtain a material that best matches experimental measurements, and this is done via easy and non-destructive poking actions. The STL files for our rigid cylinders, as well as the force and indentation poking data used in our experiments are released on our project website.

One limitation of our work is that the depth of the material is assumed to be known for optimization. We did demonstrate (Figure 26) that the correct depth can be discovered by trying different depths, and picking the one that produces the best optimization function value. However, such a process can be time-consuming. Especially for human tissue, it is better to use medical imaging (e.g., a non-invasive technique such as ultrasound) to determine the depth. Our poking method assumes that the object under the poking site is homogeneous. Because the musculoskeletal tissues in the human body are quite diverse (fat, muscles, skin, tendons, etc.) and their material properties vary spatially (e.g., they are layered), our poking method is less precise for human tissues. In the future, we would like to combine medical imaging with our systematic poking to more correctly resolve the material layers (skin, fat, muscles) in the human body. Our force data consists of a single total contact force reading; in the future, it may be possible to insert a pressure sensor under the rigid cylinder to measure and optimize a pressure distribution. That said, the presence of such sensors may somewhat alter the contact and therefore interfere with the pressure readings, or the sensors may be expensive due to their small size. Our poking is designed to recover the isotropic material and does not model friction and sliding behavior of objects. Whereas previous work

in engineering acquired incompressible Valanis-Landel materials, we model compressible materials as many objects of interest in computer graphics are compressible. While our method is able to acquire nearly incompressible materials, as demonstrated in our silicone example where the Poissons' ratio is 0.495, we do not optimize exactly incompressible materials; this is left for future work and could benefit from Mixed FEM recently proposed by [Frâncu et al. 2021]. We model material compressibility using a single parameter ($\lambda_{\text{Lamé}}$) because our poking deformation data is not rich enough to resolve more complex volume compressibility effects, i.e., more complicated functions h. A general Valanis-Landel material also has the g function, in addition to f and h. No work, including ours, has succeeded in optimizing g to the data in addition to f and h. Beyond Valanis-Landel lies the full horizon of arbitrary isotropic materials, for which new theory and experiments will need to be invented for their acquisition.

ACKNOWLEDGMENTS

REFERENCES

K. Arnavaz, M. Kragballe Nielsen, P. G. Kry, M. Macklin, and K. Erleben. 2023. Differentiable Depth for Real2Sim Calibration of Soft Body Simulations. *Computer Graphics Forum* 42, 1 (2023), 277–289.

Ellen M Arruda and Mary C Boyce. 1993. A three-dimensional constitutive model for the large stretch behavior of rubber elastic materials. *Journal of the Mechanics and Physics of Solids* 41, 2 (1993), 389–412.

Stephen W. Bailey, Dalton Omens, Paul Dilorenzo, and James F. O'Brien. 2020. Fast and Deep Facial Deformations. *ACM Trans. on Graphics (SIGGRAPH 2020)* 39, 4 (2020), 94:1–15.

Jernej Barbič, Fun Shing Sin, and Daniel Schroeder. 2012. Vega FEM Library. http://www.jernejbarbic.com/vega.

Markus Becker and Matthias Teschner. 2007. Robust and Efficient Estimation of Elasticity Parameters using the linear Finite Element Method. *Proceedings of Simulation and Visualization*, 15–28.

Kiran S. Bhat, Christopher D. Twigg, Jessica K. Hodgins, Pradeep K. Khosla, Zoran Popović, and Steven M. Seitz. 2003. Estimating Cloth Simulation Parameters from Video. In *Proceedings of Symp. on Computer Animation*. 37–51.

Bernd Bickel, Moritz Bächer, Miguel A. Otaduy, Hyunho Richard Lee, Hanspeter Pfister, Markus Gross, and Wojciech Matusik. 2010. Design and Fabrication of Materials with Desired Deformation Behavior. *ACM Trans. on Graphics (SIGGRAPH 2010)* 29, 4, Article 63 (2010), 10 pages.

B. Bickel, M. Baecher, M. Otaduy, W. Matusik, H. Pfister, and M. Gross. 2009. Capture and Modeling of Non-Linear Heterogeneous Soft Tissue. *ACM Trans. on Graphics (SIGGRAPH 2009)* 28, 3 (2009), 89:1–89:9.

J Bonet and AJ Burton. 1998. A simple orthotropic, transversely isotropic hyperelastic constitutive equation for large strain computations. *Computer methods in applied mechanics and engineering* 162, 1-4 (1998), 151–164.

Renjie Chen and Ofir Weber. 2017. GPU-Accelerated Locally Injective Shape Deformation. *ACM Trans. on Graphics (TOG)* 36, 6, Article 214 (2017), 13 pages.

Alex Choi and Yong-Ping Zheng. 2005. Estimation of Young's modulus and Poisson's ratio of soft tissue from indentation using two different-sized indentors: Finite element analysis of the finite deformation effect. *Med. Biol. Eng. Comput.* 43 (04 2005), 258–64.

David Clyde, Joseph Teran, and Rasmus Tamstorf. 2017. Modeling and Data-Driven Parameter Estimation for Woven Fabrics. In *Proceedings of Symp. on Computer Animation (SCA)*. Article 17, 11 pages.

Comsol. 2023. Comsol Multiphysics. http://www.comsol.com.

Hilmi Demiray. 1972. A note on the elasticity of soft biological tissues. *Journal of biomechanics* 5, 3 (1972), 309–311.

Mihai Frâncu, Arni Asgeirsson, Kenny Erleben, and Mads J. L. Rønnow. 2021. Locking-Proof Tetrahedra. *ACM Trans. on Graphics (TOG)* 40, 2, Article 12 (2021), 17 pages.

Xiao-Ming Fu and Yang Liu. 2016. Computing Inversion-Free Mappings by Simplex Assembly. *ACM Trans. on Graphics (SIGGRAPH Asia 2016)* 35, 6, Article 216 (2016), 12 pages.

Xiao-Ming Fu, Yang Liu, and Baining Guo. 2015. Computing Locally Injective Mappings by Advanced MIPS. *ACM Trans. on Graphics (TOG)* 34, 4, Article 71 (2015), 12 pages.

YC Fung. 1967. Elasticity of soft tissues in simple elongation. *American Journal of Physiology-Legacy Content* 213, 6 (1967), 1532–1544.

Moritz Geilinger, David Hahn, Jonas Zehnder, Moritz Bächer, Bernhard Thomaszewski, and Stelian Coros. 2020. ADD: Analytically Differentiable Dynamics for Multi-Body Systems with Frictional Contact. *ACM Trans. on Graphics (SIGGRAPH Asia 2020)* 39, 6, Article 190 (2020), 15 pages.

Alan N Gent. 1996. A new constitutive relation for rubber. *Rubber chemistry and technology* 69, 1 (1996), 59–61.

David Hahn, Pol Banzet, James M. Bern, and Stelian Coros. 2019. Real2Sim: Visco-Elastic Parameter Estimation from Dynamic Motion. *ACM Trans. on Graphics (SIGGRAPH Asia 2019)* 38, 6, Article 236 (2019), 13 pages.

David Harmon and Denis Zorin. 2013. Subspace Integration with Local Deformations. *ACM Trans. Graph.* (2013), 107:1–107:10.

ASTM International. 2021. Standard Test Method for Rubber Property-Durometer Hardness. D2240-15 Durometer Standard.

G. Irving, J. Teran, and R. Fedkiw. 2004. Invertible Finite Elements for Robust Simulation of Large Deformation. In *Symp. on Computer Animation (SCA)*. 131–140.

Krishna Murthy Jatavallabhula, Miles Macklin, Florian Golemo, Vikram Voleti, Linda Petrini, Martin Weiss, Breandan Considine, Jerome Parent-Levesque, Kevin Xie, Kenny Erleben, Liam Paull, Florian Shkurti, Derek Nowrouzezahrai, and Sanja Fidler. 2021. gradSim: Differentiable simulation for system identification and visuomotor control. arXiv:2104.02646 [cs.CV]

J.M.Ball. 1984. Differentiability Properties of Symmetric and Isotropic Functions. *Duke Math. J.* 51, 3 (1984), 699–728.

Kenneth Langstreth Johnson and Kenneth Langstreth Johnson. 1987. *Contact mechanics*. Cambridge university press.

J.S. Jurvelin, M.D. Buschmann, and E.B. Hunziker. 1997. Optical and mechanical determination of Poisson's ratio of adult bovine humeral articular cartilage. *Journal of Biomechanics* 30, 3 (1997), 235–241.

Rama Krishna Kandukuri, Jan Achterhold, Michael Möller, and Jörg Stückler. 2020. Learning to Identify Physical Parameters from Video Using Differentiable Physics. arXiv:2009.08292 [cs.CV]

M Kauer, V Vuskovic, J Dual, G Szekely, and M Bajka. 2002. Inverse finite element characterization of soft tissues. *Medical Image Analysis* 6, 3 (2002), 275–287. Special Issue on Medical Image Computing and Computer-Assisted Intervention - MICCAI 2001.

Jung Kim and Mandayam Srinivasan. 2005. Characterization of Viscoelastic Soft Tissue Properties from In Vivo Animal Experiments and Inverse FE Parameter Estimation. *International Conference on Medical Image Computing and Computer-Assisted Intervention (MICCAI)* 8, 599–606.

Luigi La Ragione, Francesco Musceo, and Alfredo Sollazzo. 2008. Axisymmetric indentation of a rigid cylinder on a layered compressible and incompressible halfspace. *Journal of Mechanics of Materials and Structures* 3, 8 (2008), 1499–1520.

Jochen Lang, Dinesh Pai, and Robert Woodham. 2002. Acquisition of Elastic Models for Interactive Simulation. *International J. of Robotics Research* 21 (2002), 713–733.

Quentin Le Lidec, Igor Kalevatykh, Ivan Laptev, Cordelia Schmid, and Justin Carpentier. 2021. Differentiable Simulation for Physical System Identification. *IEEE Robotics and Automation Letters* 6, 2 (2021), 3413–3420.

Junbang Liang, Ming Lin, and Vladlen Koltun. 2019. Differentiable Cloth Simulation for Inverse Problems. In *Advances in Neural Information Processing Systems*, Vol. 32. Curran Associates, Inc.

Ligang Liu, Chunyang Ye, Ruiqi Ni, and Xiao-Ming Fu. 2018. Progressive Parameterizations. *ACM Trans. on Graphics (SIGGRAPH 2018)* 37, 4, Article 41 (2018), 12 pages.

Eder Miguel, Derek Bradley, Bernhard Thomaszewski, Bernd Bickel, Wojciech Matusik, Miguel A. Otaduy, and Steve Marschner. 2012. Data-Driven Estimation of Cloth Simulation Models. *Computer Graphics Forum (Proc. of Eurographics)* 31, 2 (2012).

Eder Miguel, David Miraut, and Miguel A. Otaduy. 2016. Modeling and Estimation of Energy-Based Hyperelastic Objects. In *Proc. of the 37th Annual Conference of the European Association for Computer Graphics*. Eurographics Association, 385–396.

Eder Miguel, Rasmus Tamstorf, Derek Bradley, Sara C. Schvartzman, Bernhard Thomaszewski, Bernd Bickel, Wojciech Matusik, Steve Marschner, and Miguel A. Otaduy. 2013. Modeling and Estimation of Internal Friction in Cloth. *ACM Trans. on Graphics (SIGGRAPH Asia 2013)* 32, 6, Article 212 (2013), 10 pages.

Melvin Mooney. 1940. A theory of large elastic deformation. *Journal of applied physics* 11, 9 (1940), 582–592.

Matthias Müller and Markus Gross. 2004. Interactive Virtual Materials. In *Proceedings of Graphics Interface 2004* (London, Ontario, Canada) (*GI '04*). Canadian Human-Computer Communications Society, Waterloo, CAN, 239–246.

Patrizio Neff, Bernhard Eidel, and Robert Martin. 2016. Geometry of Logarithmic Strain Measures in Solid Mechanics. *Archive for Rational Mechanics and Analysis* (11 2016).

Raymond William Ogden. 1972. Large deformation isotropic elasticity–on the correlation of theory and experiment for incompressible rubberlike solids. *Proceedings of the Royal Society of London. A. Mathematical and Physical Sciences* 326, 1567 (1972), 565–584.

Dinesh K. Pai, Kees van den Doel, Doug L. James, Jochen Lang, John E. Lloyd, Joshua L. Richmond, and Som H. Yau. 2001. Scanning Physical Interaction Behavior of 3D Objects. In *Proceedings of the 28th Annual Conference on Computer Graphics and Interactive Techniques (SIGGRAPH '01)*. 87–96.

Dinesh K Pai and Peter Rizun. 2003. The WHaT: A wireless haptic texture sensor. In *11th Symposium on Haptic Interfaces for Virtual Environment and Teleoperator Systems, 2003. HAPTICS 2003. Proceedings*. IEEE, 3–9.

Dinesh K Pai, Austin Rothwell, Pearson Wyder-Hodge, Alistair Wick, Ye Fan, Egor Larionov, Darcy Harrison, Debanga Raj Neog, and Cole Shing. 2018. The human touch: measuring contact with real human soft tissues. *ACM Trans. on Graphics (Proc. of ACM SIGGRAPH 2018)* 37, 4 (2018), 58.

Mark Pauly, Dinesh K Pai, and Leonidas J Guibas. 2004. Quasi-rigid objects in contact. In *Symp. on Computer Animation (SCA)*. 109–119.

T. Payne, S. Mitchell, R. Bibb, and M. Waters. 2015. Development of novel synthetic muscle tissues for sports impact surrogates. *J. Mech. Behav. Biomed. Mater.* 41 (2015), 357–374.

MG Peutz, HP Van Kempen, and A Jones. 1968. Layered systems under normal surface loads. *Highway Research Record* 228 (1968).

W. Press, S. Teukolsky, W. Vetterling, and B. Flannery. 2007. *Numerical recipes: The art of scientific computing* (third ed.). Cambridge University Press, Cambridge, UK.

RSl Rivlin. 1948. Large elastic deformations of isotropic materials. I. Fundamental concepts. *Philosophical Transactions of the Royal Society of London. Series A, Mathematical and Physical Sciences* 240, 822 (1948), 459–490.

Christian Schumacher, Espen Knoop, and Moritz Bacher. 2020. Simulation-Ready Characterization of Soft Robotic Materials. *IEEE Robotics and Automation Letters* PP (2020), 1–1.

Agniva Sengupta, Romain Lagneau, Alexandre Krupa, Eric Marchand, and Maud Marchal. 2020. Simultaneous Tracking and Elasticity Parameter Estimation of Deformable Objects. In *2020 IEEE International Conference on Robotics and Automation (ICRA)*. 10038–10044.

Anna Shtengel, Roi Poranne, Olga Sorkine-Hornung, Shahar Z. Kovalsky, and Yaron Lipman. 2017. Geometric Optimization via Composite Majorization. *ACM Trans. on Graphics (SIGGRAPH 2017)* 36, 4, Article 38 (2017), 11 pages.

Anatolii Sianov and Matthias Harders. 2013. Data-driven haptics: Addressing inhomogeneities and computational formulation. In *2013 World Haptics Conference (WHC)*. IEEE, 301–306.

Eftychios Sifakis and Jernej Barbič. 2012. FEM simulation of 3D deformable solids: a practitioner's guide to theory, discretization and model reduction. In *ACM SIGGRAPH 2012 Courses*. ACM, 20:1–20:50.

Breannan Smith, Fernando De Goes, and Theodore Kim. 2018. Stable Neo-Hookean Flesh Simulation. *ACM Trans. Graphics (TOG)* 37, 2, Article 12 (2018), 15 pages.

Breannan Smith, Fernando De Goes, and Theodore Kim. 2019. Analytic Eigensystems for Isotropic Distortion Energies. *ACM Trans. Graphics (TOG)* 38, 1, Article 3 (2019), 15 pages.

Jason Smith and Scott Schaefer. 2015. Bijective Parameterization with Free Boundaries. *ACM Trans. on Graphics (SIGGRAPH 2015)* 34, 4, Article 70 (2015), 9 pages.

SmoothOn. 2020. SmoothOn Inc. www.smooth-on.com.

Ian N Sneddon. 1946. Boussinesq's problem for a flat-ended cylinder. In *Mathematical Proceedings of the Cambridge Philosophical Society*, Vol. 42. Cambridge University Press, 29–39.

Changkyu Song and Abdeslam Boularias. 2020. Learning to Slide Unknown Objects with Differentiable Physics Simulations. arXiv:2005.05456 [cs.RO]

Alexey Stomakhin, Russell Howes, Craig Schroeder, and Joseph M. Teran. 2012. Energetically Consistent Invertible Elasticity. In *Symp. on Computer Animation (SCA)*. 25–32.

Theodore Sussman and Klaus-Jürgen Bathe. 2009. A model of incompressible isotropic hyperelastic material behavior using spline interpolations of tension–compression test data. *Communications in Numerical Methods in Engineering* 25, 1 (2009), 53–63.

Joseph Teran, Eftychios Sifakis, Geoffrey Irving, and Ronald Fedkiw. 2005. Robust Quasistatic Finite Elements and Flesh Simulation. In *Symp. on Computer Animation (SCA)*. 181–190.

LRG Treloar. 1944. Stress-strain data for vulcanized rubber under various types of deformation. *Rubber Chemistry and Technology* 17, 4 (1944), 813–825.

KC Valanis and Robert F Landel. 1967. The strain-energy function of a hyperelastic material in terms of the extension ratios. *Journal of Applied Physics* 38, 7 (1967), 2997–3002.

DR Veronda and RA Westmann. 1970. Mechanical characterization of skin—finite deformations. *Journal of biomechanics* 3, 1 (1970), 111–124.

Bin Wang, Yuanmin Deng, Paul Kry, Uri Ascher, Hui Huang, and Baoquan Chen. 2020. Learning Elastic Constitutive Material and Damping Models. arXiv:1909.01875 [cs.GR]

Bin Wang, Longhua Wu, KangKang Yin, Uri Ascher, Libin Liu, and Hui Huang. 2015. Deformation Capture and Modeling of Soft Objects. *ACM Trans. on Graphics (SIGGRAPH 2015)* 34, 4, Article 94 (2015), 12 pages.

Huamin Wang, James O'Brien, and Ravi Ramamoorthi. 2011. Data-Driven Elastic Models for Cloth: Modeling and Measurement. *ACM Trans. on Graphics (SIGGRAPH 2011)* 30, 4 (2011), 71:1–71:12.

Cora Wex, Susann Arndt, Anke Stoll, Christiane Bruns, and Yuliya Kupriyanova. 2015. Isotropic incompressible hyperelastic models for modelling the mechanical behaviour of biological tissues: a review. *Biomedical Engineering/Biomedizinische Technik* 60, 6 (2015), 577–592.

Peter Wriggers and Tod A Laursen. 2006. *Computational contact mechanics*. Vol. 2. Springer.

Hongyi Xu, Funshing Sin, Yufeng Zhu, and Jernej Barbič. 2015. Nonlinear material design using principal stretches. *ACM Trans. on Graphics (TOG)* 34, 4 (2015), 1–11.

Shan Yang, Junbang Liang, and Ming C. Lin. 2017. Learning-Based Cloth Material Recovery from Video. In *IEEE Int. Conf. on Computer Vision (ICCV)*. 4393–4403.

Oon H Yeoh. 1990. Characterization of elastic properties of carbon-black-filled rubber vulcanizates. *Rubber chemistry and technology* 63, 5 (1990), 792–805.

Oon H Yeoh. 1993. Some forms of the strain energy function for rubber. *Rubber Chemistry and technology* 66, 5 (1993), 754–771.

Sunghoon Yim, Seokhee Jeon, and Seungmoon Choi. 2016. Data-driven haptic modeling and rendering of viscoelastic and frictional responses of deformable objects. *IEEE transactions on Haptics* 9, 4 (2016), 548–559.

Naghmeh Zamani and Heather Culbertson. 2022. Effects of Physical Hardness on the Perception of Rendered Stiffness in an Encountered-Type Haptic Display. *IEEE Transactions on Haptics* (2022), 1–10.

Ming Zhang, Y.P. Zheng, and Arthur F.T. Mak. 1997. Estimating the effective Young's modulus of soft tissues from indentation tests—nonlinear finite element analysis of effects of friction and large deformation. *Medical Engineering Physics* 19, 6 (1997), 512–517.

Yufeng Zhu. 2021. Eigen Space of Mesh Distortion Energy Hessian. (2021). arXiv:2103.08141 [cs.GR]

A MATERIALS

All materials in this section are special cases of our material, i.e., expressible in our generalized Neo-Hookean Valanis-Landel family (i.e., $g = 0$, and h is quadratic in log of volume).

A.1 Neo-Hookean Material

The energy density function is [Bonet and Burton 1998]

$$\Psi = \frac{\mu}{2}(\lambda_1^2 + \lambda_2^2 + \lambda_3^2 - 3) - \mu\log(\lambda_1\lambda_2\lambda_3) + \frac{\lambda}{2}\log^2(\lambda_1\lambda_2\lambda_3), \quad (19)$$

$$f(x) = \frac{\mu}{2}(x^2 - 1) - \mu\log(x), \quad (20)$$

$$g(x) = 0, \qquad h(x) = \frac{\lambda}{2}\log^2(x). \quad (21)$$

A.2 Hencky Material

The energy density function is [Neff et al. 2016]

$$\Psi = \mu(\log^2(\lambda_1) + \log^2(\lambda_2) + \log^2(\lambda_3)) + \frac{\lambda}{2}(\lambda_1\lambda_2\lambda_3), \quad (22)$$

$$f(x) = \mu\log^2(x), \qquad g(x) = 0, \qquad h(x) = \frac{\lambda}{2}\log^2(x). \quad (23)$$

A.3 Ogden Material

The energy density function is [Ogden 1972]

$$\Psi = \sum_{p=1}^{N} \frac{\mu_p}{\alpha_p}(\lambda_1^{\alpha_p} + \lambda_2^{\alpha_p} + \lambda_3^{\alpha_p} - 3), \quad (24)$$

$$f(x) = \sum_{p=1}^{N} \frac{\mu_p}{\alpha_p}(x^{\alpha_p} - 1), \qquad g(x) = 0, \qquad h(x) = 0. \quad (25)$$

A.4 STS Material

The energy density function is [Pai et al. 2018]

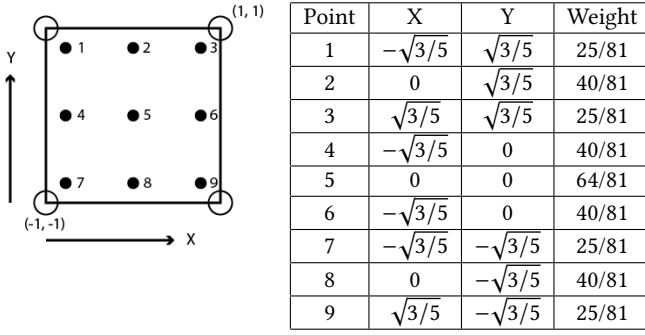| Point	X	Y	Weight
1	$-\sqrt{3/5}$	$\sqrt{3/5}$	25/81
2	0	$\sqrt{3/5}$	40/81
3	$\sqrt{3/5}$	$\sqrt{3/5}$	25/81
4	$-\sqrt{3/5}$	0	40/81
5	0	0	64/81
6	$-\sqrt{3/5}$	0	40/81
7	$-\sqrt{3/5}$	$-\sqrt{3/5}$	25/81
8	0	$-\sqrt{3/5}$	40/81
9	$\sqrt{3/5}$	$-\sqrt{3/5}$	25/81

Fig. 32. **Positions and weights of Gauss points:** Left: The 9 Gauss points positioned in one 2D mesh rectangle. Right: Positions and weights of the Gauss points.

$$\Psi_{STS} = \frac{\mu}{2}\big(\mathrm{tr}(C - I) - 2\log(J)\big) + \frac{\mu_4}{8}\,\mathrm{tr}\big((C - I)^4\big) + \frac{\lambda}{2}\log^2(J) = \tag{26}$$

$$= \frac{\mu}{2}\big(\lambda_1^2 + \lambda_2^2 + \lambda_3^2 - 3 - 2\log(\lambda_1\lambda_2\lambda_3)\big) + \tag{27}$$

$$+ \frac{\mu_4}{8}\big((\lambda_1^2 - 1)^4 + (\lambda_2^2 - 1)^4 + (\lambda_3^2 - 1)^4\big) + \frac{\lambda}{2}\log^2(\lambda_1\lambda_2\lambda_3), \tag{28}$$

$$f(x) = \mu\big(\frac{1}{2}(x^2 - 1) - \log(x)\big) + \frac{\mu_4}{8}(x^2 - 1)^4, \tag{29}$$

$$g(x) = 0, \qquad h(x) = \frac{\lambda}{2}\log^2(x). \tag{30}$$

B POSITIONS AND WEIGHTS OF GAUSS POINTS

As explained in Section 4.2, we use Gauss points (see Figure 32) to numerically integrate the 2D integral, giving us our 3D elastic energy.

C GRADIENT OF ISOTROPIC ENERGY

Given an elastic energy density function $\Psi(\lambda_1(F),\ \lambda_2(F),\ \lambda_3(F))$, it is important to compute the gradients and Hessians of Ψ with respect to the entries F_{ij} of the deformation gradient F; the gradients and Hessians are then used to calculate the internal forces and stiffness matrix, respectively. However, singularities occur in the computation of $\partial\Psi/\partial\lambda_i$ when two singular values λ_i and λ_j become the same. We show that the issue can be avoided by "chaining" the derivatives through the *lower invariants*

$$I_1 = \mathrm{tr}(S) = \lambda_1 + \lambda_2 + \lambda_3, \tag{31}$$

$$I_2 = \|F\|^2 = \lambda_1^2 + \lambda_2^2 + \lambda_3^2, \tag{32}$$

$$I_3 = \det F = \lambda_1\lambda_2\lambda_3, \tag{33}$$

where $F = RS$ is the polar decomposition, i.e., R is an orthogonal matrix, and S is a symmetric matrix. Note that the derivatives of the lower invariants with respect to the entries of F can be easily calculated, and do not suffer from any singularities. We can use the chain rule to compute the derivatives of Ψ w.r.t. F,

$$\frac{\partial\Psi}{\partial F} = \frac{\partial\Psi}{\partial(I_1,\ I_2,\ I_3)}\frac{\partial(I_1,\ I_2,\ I_3)}{\partial F}, \tag{34}$$

where

$$\frac{\partial\Psi}{\partial(\lambda_1,\ \lambda_2,\ \lambda_3)} = \frac{\partial\Psi}{\partial(I_1,\ I_2,\ I_3)}\frac{\partial(I_1,\ I_2,\ I_3)}{\partial(\lambda_1,\ \lambda_2,\ \lambda_3)}, \quad \text{i.e.} \tag{35}$$

$$(\partial_1\Psi,\ \partial_2\Psi,\ \partial_3\Psi) = \left(\frac{\partial\Psi}{\partial I_1},\ \frac{\partial\Psi}{\partial I_2},\ \frac{\partial\Psi}{\partial I_3}\right)\Xi, \tag{36}$$

where we denoted $\partial_i\Psi = \frac{\partial\Psi}{\partial\lambda_i}$ and

$$\Xi = \begin{pmatrix} 1 & 1 & 1 \\ 2\lambda_1 & 2\lambda_2 & 2\lambda_3 \\ \lambda_2\lambda_3 & \lambda_3\lambda_1 & \lambda_1\lambda_2 \end{pmatrix}. \tag{37}$$

Suppose the SVD of F is

$$F = U\,\mathrm{diag}(\lambda_1,\ \lambda_2,\ \lambda_3)\ V^T = \lambda_1\mathbf{u}_1\mathbf{v}_1^T + \lambda_2\mathbf{u}_2\mathbf{v}_2^T + \lambda_3\mathbf{u}_3\mathbf{v}_3^T,$$

where $U = (\mathbf{u}_1,\ \mathbf{u}_2,\ \mathbf{u}_3)$ and $V = (\mathbf{v}_1,\ \mathbf{v}_2,\ \mathbf{v}_3)$. Then, we have (Equations 10, 15 and 19 in [Smith et al. 2019], respectively)

$$\begin{array}{llll} \frac{\partial I_1}{\partial F} = UV^T & = & \mathbf{u}_1\mathbf{v}_1^T + \mathbf{u}_2\mathbf{v}_2^T + \mathbf{u}_3\mathbf{v}_3^T \\ \frac{\partial I_2}{\partial F} = 2F & = & 2\lambda_1\mathbf{u}_1\mathbf{v}_1^T + 2\lambda_2\mathbf{u}_2\mathbf{v}_2^T + 2\lambda_3\mathbf{u}_3\mathbf{v}_3^T \\ \frac{\partial I_3}{\partial F} & = & \lambda_2\lambda_3\mathbf{u}_1\mathbf{v}_1^T + \lambda_3\lambda_1\mathbf{u}_2\mathbf{v}_2^T + \lambda_1\lambda_2\mathbf{u}_3\mathbf{v}_3^T \end{array}.$$

The above equations can be rewritten as

$$\frac{\partial(I_1,\ I_2,\ I_3)}{\partial F} = \Xi\begin{pmatrix} \mathbf{u}_1\mathbf{v}_1^T \\ \mathbf{u}_2\mathbf{v}_2^T \\ \mathbf{u}_3\mathbf{v}_3^T \end{pmatrix}. \qquad \text{Therefore,}$$

$$\frac{\partial\Psi}{\partial F} = \frac{\partial\Psi}{\partial(I_1,\ I_2,\ I_3)}\frac{\partial(I_1,\ I_2,\ I_3)}{\partial F} =$$

$$= (\partial_1\Psi,\ \partial_2\Psi,\ \partial_3\Psi)\,\Xi^{-1}\Xi\begin{pmatrix} \mathbf{u}_1\mathbf{v}_1^T \\ \mathbf{u}_2\mathbf{v}_2^T \\ \mathbf{u}_3\mathbf{v}_3^T \end{pmatrix} =$$

$$= \partial_1\Psi\mathbf{u}_1\mathbf{v}_1^T + \partial_2\Psi\mathbf{u}_2\mathbf{v}_2^T + \partial_3\Psi\mathbf{u}_3\mathbf{v}_3^T = U\,\mathrm{diag}(\partial_1\Psi,\ \partial_2\Psi,\ \partial_3\Psi)\ V^T.$$

This even holds when two singular values are the same, say $\lambda_1 = \lambda_2 = \lambda$, since we have

$$\Psi(\lambda_1,\ \lambda_2,\ \lambda_3) = \Psi(\lambda_2,\ \lambda_1,\ \lambda_3) \Rightarrow \partial_1\Psi(\lambda_1,\ \lambda_2,\ \lambda_3) = \partial_2\Psi(\lambda_2,\ \lambda_1,\ \lambda_3),$$

which implies

$$\left.\frac{\partial\Psi}{\partial F}\right|_{\lambda_1=\lambda_2=\lambda} = \partial_1\Psi(\lambda,\ \lambda,\ \lambda_3)\left(\mathbf{u}_1\mathbf{v}_1^T + \mathbf{u}_2\mathbf{v}_2^T\right) + \partial_3\Psi(\lambda,\ \lambda,\ \lambda_3)\mathbf{u}_3\mathbf{v}_3^T.$$

C.1 Singularity Analysis

When two singular values are the same, there is an infinite number of choices for U and V, differing by a rotation:

$$\widetilde{U} = (\widetilde{\mathbf{u}}_1,\ \widetilde{\mathbf{u}}_2,\ \widetilde{\mathbf{u}}_3) = U\begin{pmatrix} \cos\theta & -\sin\theta & 0 \\ \sin\theta & \cos\theta & 0 \\ 0 & 0 & 1 \end{pmatrix},$$

$$\widetilde{V} = (\widetilde{\mathbf{v}}_1,\ \widetilde{\mathbf{v}}_2,\ \widetilde{\mathbf{v}}_3) = V\begin{pmatrix} \cos\theta & -\sin\theta & 0 \\ \sin\theta & \cos\theta & 0 \\ 0 & 0 & 1 \end{pmatrix}.$$

It follows that

$$\widetilde{\mathbf{u}}_1 \widetilde{\mathbf{v}}_1^T + \widetilde{\mathbf{u}}_2 \widetilde{\mathbf{v}}_2^T = (\widetilde{\mathbf{u}}_1, \ \widetilde{\mathbf{u}}_2) \begin{pmatrix} \widetilde{\mathbf{v}}_1^T \\ \widetilde{\mathbf{v}}_2^T \end{pmatrix} =$$

$$= (\mathbf{u}_1, \ \mathbf{u}_2) \begin{pmatrix} \cos\theta & -\sin\theta \\ \sin\theta & \cos\theta \end{pmatrix} \begin{pmatrix} \cos\theta & \sin\theta \\ -\sin\theta & \cos\theta \end{pmatrix} \begin{pmatrix} \mathbf{v}_1^T \\ \mathbf{v}_2^T \end{pmatrix} =$$

$$= (\mathbf{u}_1, \ \mathbf{u}_2) \begin{pmatrix} \mathbf{v}_1^T \\ \mathbf{v}_2^T \end{pmatrix} = \mathbf{u}_1 \mathbf{v}_1^T + \mathbf{u}_2 \mathbf{v}_2^T.$$

Thus, the expression for $\frac{\partial \Psi}{\partial F}$ remains the same when using a different pair of U, V.

Similarly, when all three singular values are the same, i.e. $\lambda_1 = \lambda_2 = \lambda_3$, we have

$$\left. \frac{\partial \Psi}{\partial F} \right|_{\lambda_1 = \lambda_2 = \lambda_3 = \lambda} = \partial_1 \Psi(\lambda, \ \lambda, \ \lambda) \left(\mathbf{u}_1 \mathbf{v}_1^T + \mathbf{u}_2 \mathbf{v}_2^T + \mathbf{u}_3 \mathbf{v}_3^T \right),$$

which is independent of the choice of U, V since different U, V differ by the same orthogonal matrix.

D HESSIAN OF ISOTROPIC ENERGY

For second derivatives, differentiate the following expression:

$$\frac{\partial \Psi}{\partial F} = \frac{\partial \Psi}{\partial (I_1, \ I_2, \ I_3)} \frac{\partial (I_1, \ I_2, \ I_3)}{\partial F},$$

$$\Rightarrow \frac{\partial^2 \Psi}{\partial F^2} = \left(\frac{\partial (I_1, \ I_2, \ I_3)}{\partial F} \right)^T \frac{\partial^2 \Psi}{\partial (I_1, \ I_2, \ I_3)^2} \frac{\partial (I_1, \ I_2, \ I_3)}{\partial F} +$$

$$+ \frac{\partial \Psi}{\partial (I_1, \ I_2, \ I_3)} \frac{\partial^2 (I_1, \ I_2, \ I_3)}{\partial F^2},$$

where all of the terms are already known except $\partial^2 \Psi / \partial (I_1, \ I_2, \ I_3)^2$. Note that

$$\frac{\partial^2 \Psi}{\partial (\lambda_1, \ \lambda_2, \ \lambda_3)^2} = \left(\frac{\partial (I_1, \ I_2, \ I_3)}{\partial (\lambda_1, \ \lambda_2, \ \lambda_3)} \right)^T \frac{\partial^2 \Psi}{\partial (I_1, \ I_2, \ I_3)^2} \frac{\partial (I_1, \ I_2, \ I_3)}{\partial (\lambda_1, \ \lambda_2, \ \lambda_3)} +$$

$$\frac{\partial \Psi}{\partial (I_1, \ I_2, \ I_3)} \frac{\partial^2 (I_1, \ I_2, \ I_3)}{\partial (\lambda_1, \ \lambda_2, \ \lambda_3)^2}, \qquad \text{thus}$$

$$\frac{\partial^2 \Psi}{\partial (I_1, \ I_2, \ I_3)^2} = \left(\frac{\partial (I_1, \ I_2, \ I_3)}{\partial (\lambda_1, \ \lambda_2, \ \lambda_3)} \right)^{-T} \left(\frac{\partial^2 \Psi}{\partial (\lambda_1, \ \lambda_2, \ \lambda_3)^2} - \right.$$

$$\left. \frac{\partial \Psi}{\partial (I_1, \ I_2, \ I_3)} \frac{\partial^2 (I_1, \ I_2, \ I_3)}{\partial (\lambda_1, \ \lambda_2, \ \lambda_3)^2} \right) \left(\frac{\partial (I_1, \ I_2, \ I_3)}{\partial (\lambda_1, \ \lambda_2, \ \lambda_3)} \right)^{-1}.$$

Since we also have

$$\frac{\partial (I_1, \ I_2, \ I_3)}{\partial F} = \left(\frac{\partial (I_1, \ I_2, \ I_3)}{\partial (\lambda_1, \ \lambda_2, \ \lambda_3)} \right) \begin{pmatrix} \mathbf{u}_1 \mathbf{v}_1^T \\ \mathbf{u}_2 \mathbf{v}_2^T \\ \mathbf{u}_3 \mathbf{v}_3^T \end{pmatrix},$$

it follows that

$$\frac{\partial^2 \Psi}{\partial F^2} = \left(\mathbf{u}_1 \mathbf{v}_1^T, \ \mathbf{u}_2 \mathbf{v}_2^T, \ \mathbf{u}_3 \mathbf{v}_3^T \right) K \begin{pmatrix} \mathbf{u}_1 \mathbf{v}_1^T \\ \mathbf{u}_2 \mathbf{v}_2^T \\ \mathbf{u}_3 \mathbf{v}_3^T \end{pmatrix} + \frac{\partial \Psi}{\partial (I_1, \ I_2, \ I_3)} \frac{\partial^2 (I_1, \ I_2, \ I_3)}{\partial F^2},$$

where

$$K = \frac{\partial^2 \Psi}{\partial (\lambda_1, \ \lambda_2, \ \lambda_3)^2} - \frac{\partial \Psi}{\partial (I_1, \ I_2, \ I_3)} \frac{\partial^2 (I_1, \ I_2, \ I_3)}{\partial (\lambda_1, \ \lambda_2, \ \lambda_3)^2} =$$

$$= \frac{\partial^2 \Psi}{\partial (\lambda_1, \ \lambda_2, \ \lambda_3)^2} - 2I \frac{\partial \Psi}{\partial I_2} - Q \frac{\partial \Psi}{\partial I_3},$$

$$Q = \frac{\partial^2 I_3}{\partial (\lambda_1, \ \lambda_2, \ \lambda_3)^2} = \begin{pmatrix} 0 & \lambda_3 & \lambda_2 \\ \lambda_3 & 0 & \lambda_1 \\ \lambda_2 & \lambda_1 & 0 \end{pmatrix}.$$

For the second term in $\frac{\partial^2 \Psi}{\partial F^2}$, we need Hessians of I_1, I_2, I_3 with respect to F. Suppose we have a function to unroll a 3×3 matrix into a 9-dim vector; call it $vec : \mathbb{R}^{3 \times 3} \rightarrow \mathbb{R}^9$. Then, the following nine vectors constitute an orthonormal basis of $\mathbb{R}^9$:

$$\begin{array}{lll}
\mathbf{d}_1 = \text{vec}\left(\mathbf{u}_1 \mathbf{v}_1^T\right) & \mathbf{t}_1 = \frac{\text{vec}(\mathbf{u}_3 \mathbf{v}_2^T - \mathbf{u}_2 \mathbf{v}_3^T)}{\sqrt{2}} & \mathbf{l}_1 = \frac{\text{vec}(\mathbf{u}_3 \mathbf{v}_2^T + \mathbf{u}_2 \mathbf{v}_3^T)}{\sqrt{2}} \\
\mathbf{d}_2 = \text{vec}\left(\mathbf{u}_2 \mathbf{v}_2^T\right), & \mathbf{t}_2 = \frac{\text{vec}(\mathbf{u}_1 \mathbf{v}_3^T - \mathbf{u}_3 \mathbf{v}_1^T)}{\sqrt{2}}, & \mathbf{l}_2 = \frac{\text{vec}(\mathbf{u}_1 \mathbf{v}_3^T + \mathbf{u}_3 \mathbf{v}_1^T)}{\sqrt{2}}. \\
\mathbf{d}_3 = \text{vec}\left(\mathbf{u}_3 \mathbf{v}_3^T\right) & \mathbf{t}_3 = \frac{\text{vec}(\mathbf{u}_2 \mathbf{v}_1^T - \mathbf{u}_1 \mathbf{v}_2^T)}{\sqrt{2}} & \mathbf{l}_3 = \frac{\text{vec}(\mathbf{u}_2 \mathbf{v}_1^T + \mathbf{u}_1 \mathbf{v}_2^T)}{\sqrt{2}}
\end{array}$$

Then $\frac{\partial^2 (I_1, I_2, I_3)}{\partial F^2}$ can be simply expressed in this basis [Smith et al. 2019]

$$\frac{\partial^2 I_1}{\partial F^2} = (\mathbf{t}_1, \ \mathbf{t}_2, \ \mathbf{t}_3) A \begin{pmatrix} \mathbf{t}_1^T \\ \mathbf{t}_2^T \\ \mathbf{t}_3^T \end{pmatrix}, \quad \frac{\partial^2 I_2}{\partial F^2} = 2I,$$

$$\frac{\partial^2 I_3}{\partial F^2} = (\mathbf{d}_1, \ \mathbf{d}_2, \ \mathbf{d}_3) Q \begin{pmatrix} \mathbf{d}_1^T \\ \mathbf{d}_2^T \\ \mathbf{d}_3^T \end{pmatrix} + (\mathbf{t}_1, \ \mathbf{t}_2, \ \mathbf{t}_3) \Lambda \begin{pmatrix} \mathbf{t}_1^T \\ \mathbf{t}_2^T \\ \mathbf{t}_3^T \end{pmatrix} - (\mathbf{l}_1, \ \mathbf{l}_2, \ \mathbf{l}_3) \Lambda \begin{pmatrix} \mathbf{l}_1^T \\ \mathbf{l}_2^T \\ \mathbf{l}_3^T \end{pmatrix},$$

where

$$A = \text{diag}\left(\frac{2}{\lambda_2 + \lambda_3}, \ \frac{2}{\lambda_3 + \lambda_1}, \ \frac{2}{\lambda_1 + \lambda_2} \right), \quad \Lambda = diag(\lambda_1, \ \lambda_2, \ \lambda_3).$$

Therefore, the Hessian of Ψ can be simply represented as follows:

$$\frac{\partial^2 \Psi}{\partial F^2} = B \begin{pmatrix} H_1 & 0 & 0 \\ 0 & H_2 & 0 \\ 0 & 0 & H_3 \end{pmatrix} B^T, \qquad \text{where}$$

$$B = (\mathbf{d}_1, \ \mathbf{d}_2, \ \mathbf{d}_3, \ \mathbf{t}_1, \ \mathbf{t}_2, \ \mathbf{t}_3, \ \mathbf{l}_1, \ \mathbf{l}_2, \ \mathbf{l}_3),$$

$$H_1 = K + 2I \frac{\partial \Psi}{\partial I_2} + Q \frac{\partial \Psi}{\partial I_3} = \frac{\partial^2 \Psi}{\partial (\lambda_1, \ \lambda_2, \ \lambda_3)^2},$$

$$H_2 = A \frac{\partial \Psi}{\partial I_1} + 2I \frac{\partial \Psi}{\partial I_2} + \Lambda \frac{\partial \Psi}{\partial I_3} =$$

$$= (E_{11}, \ E_{22}, \ E_{33}) \begin{pmatrix} \frac{2}{\lambda_2 + \lambda_3} & 2 & \lambda_1 \\ \frac{2}{\lambda_3 + \lambda_1} & 2 & \lambda_2 \\ \frac{2}{\lambda_1 + \lambda_2} & 2 & \lambda_3 \end{pmatrix} \begin{pmatrix} 1 & 2\lambda_1 & \lambda_2 \lambda_3 \\ 1 & 2\lambda_2 & \lambda_3 \lambda_1 \\ 1 & 2\lambda_3 & \lambda_1 \lambda_2 \end{pmatrix}^{-1} \begin{pmatrix} \partial_1 \Psi \\ \partial_2 \Psi \\ \partial_3 \Psi \end{pmatrix} =$$

$$= \text{diag}\left(\frac{\partial_2 \Psi + \partial_3 \Psi}{\lambda_2 + \lambda_3}, \ \frac{\partial_3 \Psi + \partial_1 \Psi}{\lambda_3 + \lambda_1}, \ \frac{\partial_1 \Psi + \partial_2 \Psi}{\lambda_1 + \lambda_2} \right),$$

$$H_3 = 2I \frac{\partial \Psi}{\partial I_2} - \Lambda \frac{\partial \Psi}{\partial I_3} =$$

$$= (E_{11}, \ E_{22}, \ E_{33}) \begin{pmatrix} 0 & 2 & -\lambda_1 \\ 0 & 2 & -\lambda_2 \\ 0 & 2 & -\lambda_3 \end{pmatrix} \begin{pmatrix} 1 & 2\lambda_1 & \lambda_2 \lambda_3 \\ 1 & 2\lambda_2 & \lambda_3 \lambda_1 \\ 1 & 2\lambda_3 & \lambda_1 \lambda_2 \end{pmatrix}^{-1} \begin{pmatrix} \partial_1 \Psi \\ \partial_2 \Psi \\ \partial_3 \Psi \end{pmatrix} =$$

$$= \text{diag}\left(\frac{\partial_2 \Psi - \partial_3 \Psi}{\lambda_2 - \lambda_3}, \ \frac{\partial_3 \Psi - \partial_1 \Psi}{\lambda_3 - \lambda_1}, \ \frac{\partial_1 \Psi - \partial_2 \Psi}{\lambda_1 - \lambda_2} \right).$$

Here, E_{ij} refers to the 3×3 matrix where the (i, j) entry is 1 and others are 0. In conclusion, in basis B, the Hessian is a 9×9 block-diagonal matrix with one block of size 3×3 and six blocks of size 1×1 (also shown in Figure 6)

$$\frac{\partial^2 \Psi}{\partial F^2} = B \, \text{diag} \left(\begin{pmatrix} \partial_{11}\Psi & \partial_{12}\Psi & \partial_{13}\Psi \\ \partial_{12}\Psi & \partial_{22}\Psi & \partial_{23}\Psi \\ \partial_{13}\Psi & \partial_{23}\Psi & \partial_{33}\Psi \end{pmatrix}, \right.$$

$$\frac{\partial_2\Psi + \partial_3\Psi}{\lambda_2 + \lambda_3}, \frac{\partial_3\Psi + \partial_1\Psi}{\lambda_3 + \lambda_1}, \frac{\partial_1\Psi + \partial_2\Psi}{\lambda_1 + \lambda_2},$$

$$\left. \frac{\partial_2\Psi - \partial_3\Psi}{\lambda_2 - \lambda_3}, \frac{\partial_3\Psi - \partial_1\Psi}{\lambda_3 - \lambda_1}, \frac{\partial_1\Psi - \partial_2\Psi}{\lambda_1 - \lambda_2} \right) B^T =$$

$$= (\mathbf{d}_1, \, \mathbf{d}_2, \, \mathbf{d}_3) \frac{\partial^2 \Psi}{\partial (\lambda_1, \, \lambda_2, \, \lambda_3)^2} \begin{pmatrix} \mathbf{d}_1^T \\ \mathbf{d}_2^T \\ \mathbf{d}_3^T \end{pmatrix} + \frac{\partial_2\Psi + \partial_3\Psi}{\lambda_2 + \lambda_3} \mathbf{t}_1 \mathbf{t}_1^T +$$

$$+ \frac{\partial_3\Psi + \partial_1\Psi}{\lambda_3 + \lambda_1} \mathbf{t}_2 \mathbf{t}_2^T + \frac{\partial_1\Psi + \partial_2\Psi}{\lambda_1 + \lambda_2} \mathbf{t}_3 \mathbf{t}_3^T + \frac{\partial_2\Psi - \partial_3\Psi}{\lambda_2 - \lambda_3} \mathbf{l}_1 \mathbf{l}_1^T +$$

$$+ \frac{\partial_3\Psi - \partial_1\Psi}{\lambda_3 - \lambda_1} \mathbf{l}_2 \mathbf{l}_2^T + \frac{\partial_1\Psi - \partial_2\Psi}{\lambda_1 - \lambda_2} \mathbf{l}_3 \mathbf{l}_3^T.$$

Projection to SPD is now readily available. The upper-left 3×3 block can be projected by performing an eigendecomposition and clamping the eigenvalues to non-negative values (or small positive values). The other Hessian blocks are all scalars and can be trivially projected to non-negativity (or small positivity). However, divisions by zero may appear in the Hessian diagonal blocks when two or three singular values are the same. These are removable singularities, and we show how to handle them next.

D.1 Singularity Analysis

When the energy is isotropic and two eigenvalues become very close, say λ_1 and λ_2, all of the above terms work well except $\frac{\partial_1\Psi - \partial_2\Psi}{\lambda_1 - \lambda_2}$, which can be expanded using a Taylor series for fixed λ_2, λ_3 in terms of λ_1, around $\lambda_1 = \lambda_2$:

$$\frac{\partial_1\Psi - \partial_2\Psi}{\lambda_1 - \lambda_2} = \frac{1}{\lambda_1 - \lambda_2} \sum_{k=0}^{+\infty} \frac{(\lambda_1 - \lambda_2)^k}{k!} \partial_1^k (\partial_1 - \partial_2) \Psi (\lambda_2, \, \lambda_2, \, \lambda_3) =$$

$$= \sum_{k=0}^{+\infty} \frac{(\lambda_1 - \lambda_2)^k}{(k+1)!} \partial_1^{k+1} (\partial_1 - \partial_2) \Psi (\lambda_2, \, \lambda_2, \, \lambda_3).$$

The last equality holds because the constant term in the above expansion is zero, due to the symmetry $\partial_1\Psi (\lambda_2, \, \lambda_2, \, \lambda_3) = \partial_2\Psi (\lambda_2, \, \lambda_2, \, \lambda_3)$. In other words, the singularity is removable. When $\lambda_1 = \lambda_2$, we have:

$$\partial_1\Psi = \partial_2\Psi, \quad \partial_{11}\Psi = \partial_{22}\Psi, \quad \partial_{13}\Psi = \partial_{23}\Psi, \qquad \text{as well as}$$

$$\lim_{\lambda_1 \to \lambda_2} \frac{\partial_1\Psi - \partial_2\Psi}{\lambda_1 - \lambda_2} = \partial_{11}\Psi - \partial_{12}\Psi.$$

Therefore, when $\lambda_1 = \lambda_2$, the Hessian can be expressed using the following formula, which is free of singularities:

$$\frac{\partial^2 \Psi}{\partial F^2} = \partial_{11}\Psi \left(\mathbf{d}_1 \mathbf{d}_1^T + \mathbf{d}_2 \mathbf{d}_2^T + \mathbf{l}_3 \mathbf{l}_3^T \right) + \partial_{12}\Psi \left(\mathbf{d}_1 \mathbf{d}_2^T + \mathbf{d}_2 \mathbf{d}_1^T - \mathbf{l}_3 \mathbf{l}_3^T \right) +$$

$$+ \partial_{33}\Psi \mathbf{d}_3 \mathbf{d}_3^T + \frac{1}{\lambda_1} \partial_1\Psi \, \mathbf{t}_3 \mathbf{t}_3^T + \partial_{13}\Psi \left((\mathbf{d}_1 + \mathbf{d}_2) \, \mathbf{d}_3^T + \mathbf{d}_3 \left(\mathbf{d}_1^T + \mathbf{d}_2^T \right) \right) +$$

$$+ \frac{\partial_1\Psi + \partial_3\Psi}{\lambda_1 + \lambda_3} \left(\mathbf{t}_1 \mathbf{t}_1^T + \mathbf{t}_2 \mathbf{t}_2^T \right) + \frac{\partial_1\Psi - \partial_3\Psi}{\lambda_1 - \lambda_3} \left(\mathbf{l}_1 \mathbf{l}_1^T + \mathbf{l}_2 \mathbf{l}_2^T \right).$$

We activate the above formula if two singular values (but not all three) are within 10^{-4} of each other. Such an absolute threshold works because singular values are principal stretches, and for real materials in our experiments, they do *not* deviate away from 1 by orders magnitude, e.g., they stay on the $[1/2, 3/2]$ interval.

We will now show that the above formula is independent of the choice of U and V. Suppose we choose a different pair of U, V:

$$\widetilde{U} = (\widetilde{\mathbf{u}}_1, \, \widetilde{\mathbf{u}}_2, \, \widetilde{\mathbf{u}}_3) = U \begin{pmatrix} \cos\theta & -\sin\theta & 0 \\ \sin\theta & \cos\theta & 0 \\ 0 & 0 & 1 \end{pmatrix},$$

$$\widetilde{V} = (\widetilde{\mathbf{v}}_1, \, \widetilde{\mathbf{v}}_2, \, \widetilde{\mathbf{v}}_3) = V \begin{pmatrix} \cos\theta & -\sin\theta & 0 \\ \sin\theta & \cos\theta & 0 \\ 0 & 0 & 1 \end{pmatrix}.$$

Then, we have

$$\widetilde{\mathbf{d}}_1 = \mathbf{d}_1 \cos^2\theta + \mathbf{d}_2 \sin^2\theta + \sqrt{2}\mathbf{l}_3 \sin\theta \cos\theta$$

$$\widetilde{\mathbf{d}}_2 = \mathbf{d}_1 \sin^2\theta + \mathbf{d}_2 \cos^2\theta - \sqrt{2}\mathbf{l}_3 \sin\theta \cos\theta$$

$$\widetilde{\mathbf{d}}_3 = \mathbf{d}_3$$

$$\widetilde{\mathbf{t}}_1 = \mathbf{t}_1 \cos\theta - \mathbf{t}_2 \sin\theta$$

$$\widetilde{\mathbf{t}}_2 = \mathbf{t}_1 \sin\theta + \mathbf{t}_2 \cos\theta$$

$$\widetilde{\mathbf{t}}_3 = \mathbf{t}_3$$

$$\widetilde{\mathbf{l}}_1 = \mathbf{l}_1 \cos\theta - \mathbf{l}_2 \sin\theta$$

$$\widetilde{\mathbf{l}}_2 = \mathbf{l}_1 \sin\theta + \mathbf{l}_2 \cos\theta$$

$$\widetilde{\mathbf{l}}_3 = \sqrt{2} \, (\mathbf{d}_2 - \mathbf{d}_1) \sin\theta \cos\theta + \mathbf{l}_3 \left(\cos^2\theta - \sin^2\theta \right).$$

Therefore, we derive that

$$\widetilde{\mathbf{d}}_1 + \widetilde{\mathbf{d}}_2 = \mathbf{d}_1 + \mathbf{d}_2, \quad \widetilde{\mathbf{d}}_3 \widetilde{\mathbf{d}}_3^T = \mathbf{d}_3 \mathbf{d}_3^T, \quad \widetilde{\mathbf{t}}_3 \widetilde{\mathbf{t}}_3^T = \mathbf{t}_3 \mathbf{t}_3^T,$$

$$\widetilde{\mathbf{t}}_1 \widetilde{\mathbf{t}}_1^T + \widetilde{\mathbf{t}}_2 \widetilde{\mathbf{t}}_2^T = \mathbf{t}_1 \mathbf{t}_1^T + \mathbf{t}_2 \mathbf{t}_2^T, \quad \widetilde{\mathbf{l}}_1 \widetilde{\mathbf{l}}_1^T + \widetilde{\mathbf{l}}_2 \widetilde{\mathbf{l}}_2^T = \mathbf{l}_1 \mathbf{l}_1^T + \mathbf{l}_2 \mathbf{l}_2^T,$$

$$\widetilde{\mathbf{d}}_1 \widetilde{\mathbf{d}}_1^T + \widetilde{\mathbf{d}}_2 \widetilde{\mathbf{d}}_2^T + \widetilde{\mathbf{l}}_3 \widetilde{\mathbf{l}}_3^T = \mathbf{d}_1 \mathbf{d}_1^T + \mathbf{d}_2 \mathbf{d}_2^T + \mathbf{l}_3 \mathbf{l}_3^T,$$

$$\widetilde{\mathbf{d}}_1 \widetilde{\mathbf{d}}_2^T + \widetilde{\mathbf{d}}_2 \widetilde{\mathbf{d}}_1^T - \widetilde{\mathbf{l}}_3 \widetilde{\mathbf{l}}_3^T = \mathbf{d}_1 \mathbf{d}_2^T + \mathbf{d}_2 \mathbf{d}_1^T - \mathbf{l}_3 \mathbf{l}_3^T,$$

which implies that the expression for $\partial^2\Psi / \partial F^2$ is independent of the choice of U and V.

When all singular values are equal ($\lambda_1 = \lambda_2 = \lambda_3 = \lambda$), we have

$$\partial_1\Psi = \partial_2\Psi = \partial_3\Psi, \quad \partial_{11}\Psi = \partial_{22}\Psi = \partial_{33}\Psi, \quad \partial_{12}\Psi = \partial_{13}\Psi = \partial_{23}\Psi,$$

as well as

$$\lim_{\lambda_1 \to \lambda_2} \frac{\partial_1\Psi - \partial_2\Psi}{\lambda_1 - \lambda_2} = \lim_{\lambda_2 \to \lambda_3} \frac{\partial_2\Psi - \partial_3\Psi}{\lambda_2 - \lambda_3} = \lim_{\lambda_3 \to \lambda_1} \frac{\partial_3\Psi - \partial_1\Psi}{\lambda_3 - \lambda_1} =$$

$$= \partial_{11}\Psi - \partial_{12}\Psi.$$

This gives us a formula for the Hessian when $\lambda_1 = \lambda_2 = \lambda_3$, which is free of singularities:

$$\frac{\partial^2 \Psi}{\partial F^2} = \frac{1}{\lambda} \partial_1\Psi \left(\mathbf{t}_1 \mathbf{t}_1^T + \mathbf{t}_2 \mathbf{t}_2^T + \mathbf{t}_3 \mathbf{t}_3^T \right) +$$

$$+ \partial_{11}\Psi \left(\mathbf{d}_1 \mathbf{d}_1^T + \mathbf{d}_2 \mathbf{d}_2^T + \mathbf{d}_3 \mathbf{d}_3^T + \mathbf{l}_1 \mathbf{l}_1^T + \mathbf{l}_2 \mathbf{l}_2^T + \mathbf{l}_3 \mathbf{l}_3^T \right) +$$

$$+ \partial_{12}\Psi \Big(\mathbf{d}_1 \mathbf{d}_2^T + \mathbf{d}_2 \mathbf{d}_1^T + \mathbf{d}_2 \mathbf{d}_3^T +$$

$$\mathbf{d}_3 \mathbf{d}_2^T + \mathbf{d}_3 \mathbf{d}_1^T + \mathbf{d}_1 \mathbf{d}_3^T - \mathbf{l}_1 \mathbf{l}_1^T - \mathbf{l}_2 \mathbf{l}_2^T - \mathbf{l}_3 \mathbf{l}_3^T \Big).$$

We activate the above formula if all three singular values are within 10^{-4} of each other. Now, let us prove that the formula is independent of the choice of U and V. Suppose we choose a different pair of U, V:

$$\widetilde{U} = (\widetilde{\mathbf{u}_1}, \widetilde{\mathbf{u}_2}, \widetilde{\mathbf{u}_3}) = UX, \quad \widetilde{V} = (\widetilde{\mathbf{v}_1}, \widetilde{\mathbf{v}_2}, \widetilde{\mathbf{v}_3}) = VX,$$

where $X = \left(x_{ij}\right)_{i,j=1}^{3}$ is an orthogonal matrix. Then, we have

$$\widetilde{D} = \left(\widetilde{\mathbf{d}_1}, \widetilde{\mathbf{d}_2}, \widetilde{\mathbf{d}_3}\right) = (\mathbf{d}_1, \mathbf{d}_2, \mathbf{d}_3)\begin{pmatrix} x_{11}^2 & x_{12}^2 & x_{13}^2 \\ x_{21}^2 & x_{22}^2 & x_{23}^2 \\ x_{31}^2 & x_{32}^2 & x_{33}^2 \end{pmatrix} +$$

$$+\sqrt{2}\,(\mathbf{l}_1, \mathbf{l}_2, \mathbf{l}_3)\begin{pmatrix} x_{21}x_{31} & x_{22}x_{32} & x_{23}x_{33} \\ x_{31}x_{11} & x_{32}x_{12} & x_{33}x_{13} \\ x_{11}x_{21} & x_{12}x_{22} & x_{13}x_{23} \end{pmatrix} = DA_{\text{DD}} + LA_{\text{DL}},$$

$$\widetilde{T} = \left(\widetilde{\mathbf{t}_1}, \widetilde{\mathbf{t}_2}, \widetilde{\mathbf{t}_3}\right) = TA_{\text{TT}} =$$

$$= (\mathbf{t}_1, \mathbf{t}_2, \mathbf{t}_3)\begin{pmatrix} x_{33}x_{22} - x_{32}x_{23} & x_{31}x_{23} - x_{33}x_{21} & x_{32}x_{21} - x_{31}x_{22} \\ x_{13}x_{32} - x_{12}x_{33} & x_{11}x_{33} - x_{13}x_{31} & x_{12}x_{31} - x_{11}x_{32} \\ x_{23}x_{12} - x_{22}x_{13} & x_{21}x_{13} - x_{23}x_{11} & x_{22}x_{11} - x_{21}x_{12} \end{pmatrix},$$

$$\widetilde{L} = \left(\widetilde{\mathbf{l}_1}, \widetilde{\mathbf{l}_2}, \widetilde{\mathbf{l}_3}\right) =$$

$$= (\mathbf{l}_1, \mathbf{l}_2, \mathbf{l}_3)\begin{pmatrix} x_{33}x_{22} + x_{32}x_{23} & x_{31}x_{23} + x_{33}x_{21} & x_{32}x_{21} + x_{31}x_{22} \\ x_{13}x_{32} + x_{12}x_{33} & x_{11}x_{33} + x_{13}x_{31} & x_{12}x_{31} + x_{11}x_{32} \\ x_{23}x_{12} + x_{22}x_{13} & x_{21}x_{13} + x_{23}x_{11} & x_{22}x_{11} + x_{21}x_{12} \end{pmatrix} +$$

$$+\sqrt{2}\,(\mathbf{d}_1, \mathbf{d}_2, \mathbf{d}_3)\begin{pmatrix} x_{12}x_{13} & x_{13}x_{11} & x_{11}x_{12} \\ x_{22}x_{23} & x_{23}x_{21} & x_{21}x_{22} \\ x_{32}x_{33} & x_{33}x_{31} & x_{31}x_{32} \end{pmatrix} = LA_{\text{LL}} + DA_{\text{LD}}.$$

Therefore, $\widetilde{\mathbf{d}_1}\widetilde{\mathbf{d}_1}^T + \widetilde{\mathbf{d}_2}\widetilde{\mathbf{d}_2}^T + \widetilde{\mathbf{d}_3}\widetilde{\mathbf{d}_3}^T + \widetilde{\mathbf{l}_1}\widetilde{\mathbf{l}_1}^T + \widetilde{\mathbf{l}_2}\widetilde{\mathbf{l}_2}^T + \widetilde{\mathbf{l}_3}\widetilde{\mathbf{l}_3}^T =$

$$= \widetilde{D}\widetilde{D}^T + \widetilde{L}\widetilde{L}^T = (D, L)\begin{pmatrix} A_{\text{DD}} & A_{\text{LD}} \\ A_{\text{DL}} & A_{\text{LL}} \end{pmatrix}\begin{pmatrix} A_{\text{DD}}^T & A_{\text{DL}}^T \\ A_{\text{LD}}^T & A_{\text{LL}}^T \end{pmatrix}\begin{pmatrix} D^T \\ L^T \end{pmatrix} =$$

$$= (D, L)\begin{pmatrix} I & 0 \\ 0 & I \end{pmatrix}\begin{pmatrix} D^T \\ L^T \end{pmatrix} = DD^T + LL^T =$$

$$= \mathbf{d}_1\mathbf{d}_1^T + \mathbf{d}_2\mathbf{d}_2^T + \mathbf{d}_3\mathbf{d}_3^T + \mathbf{l}_1\mathbf{l}_1^T + \mathbf{l}_2\mathbf{l}_2^T + \mathbf{l}_3\mathbf{l}_3^T,$$

$$\widetilde{\mathbf{d}_1}\widetilde{\mathbf{d}_2}^T + \widetilde{\mathbf{d}_2}\widetilde{\mathbf{d}_1}^T + \widetilde{\mathbf{d}_2}\widetilde{\mathbf{d}_3}^T + \widetilde{\mathbf{d}_3}\widetilde{\mathbf{d}_2}^T + \widetilde{\mathbf{d}_3}\widetilde{\mathbf{d}_1}^T +$$

$$+\widetilde{\mathbf{d}_1}\widetilde{\mathbf{d}_3}^T - \widetilde{\mathbf{l}_1}\widetilde{\mathbf{l}_1}^T - \widetilde{\mathbf{l}_2}\widetilde{\mathbf{l}_2}^T - \widetilde{\mathbf{l}_3}\widetilde{\mathbf{l}_3}^T =$$

$$= \left(\widetilde{D}, \widetilde{L}\right)\begin{pmatrix} 0 & 1 & 1 & \\ 1 & 0 & 1 & 0 \\ 1 & 1 & 0 & \\ & 0 & & -I \end{pmatrix}\begin{pmatrix} \widetilde{D}^T \\ \widetilde{L}^T \end{pmatrix} =$$

$$= (D, L)\begin{pmatrix} A_{\text{DD}} & A_{\text{LD}} \\ A_{\text{DL}} & A_{\text{LL}} \end{pmatrix}\begin{pmatrix} 0 & 1 & 1 & \\ 1 & 0 & 1 & 0 \\ 1 & 1 & 0 & \\ & 0 & & -I \end{pmatrix}\begin{pmatrix} A_{\text{DD}}^T & A_{\text{DL}}^T \\ A_{\text{LD}}^T & A_{\text{LL}}^T \end{pmatrix}\begin{pmatrix} D^T \\ L^T \end{pmatrix} =$$

$$= (D, L)\begin{pmatrix} 0 & 1 & 1 & \\ 1 & 0 & 1 & 0 \\ 1 & 1 & 0 & \\ & 0 & & -I \end{pmatrix}\begin{pmatrix} D^T \\ L^T \end{pmatrix} =$$

$$= \mathbf{d}_1\mathbf{d}_2^T + \mathbf{d}_2\mathbf{d}_1^T + \mathbf{d}_2\mathbf{d}_3^T + \mathbf{d}_3\mathbf{d}_2^T + \mathbf{d}_3\mathbf{d}_1^T + \mathbf{d}_1\mathbf{d}_3^T - \mathbf{l}_1\mathbf{l}_1^T - \mathbf{l}_2\mathbf{l}_2^T - \mathbf{l}_3\mathbf{l}_3^T,$$

$$\sum_{i=1}^{3}\widetilde{\mathbf{t}_i}\widetilde{\mathbf{t}_i}^T = \widetilde{T}\widetilde{T}^T = TA_{\text{TT}}A_{\text{TT}}^T T^T = TT^T = \sum_{i=1}^{3}\mathbf{t}_i\mathbf{t}_i^T.$$

In the above algebraic manipulations for the $\lambda_1 = \lambda_2 = \lambda_3$ case, we used the following three Lemmas.

Lemma 1 A_{TT} is orthogonal.
Proof: Note that

$$A_{\text{TT}} = \begin{pmatrix} x_{33}x_{22} - x_{32}x_{23} & x_{31}x_{23} - x_{33}x_{21} & x_{32}x_{21} - x_{31}x_{22} \\ x_{13}x_{32} - x_{12}x_{33} & x_{11}x_{33} - x_{13}x_{31} & x_{12}x_{31} - x_{11}x_{32} \\ x_{23}x_{12} - x_{22}x_{13} & x_{21}x_{13} - x_{23}x_{11} & x_{22}x_{11} - x_{21}x_{12} \end{pmatrix} =$$

$$(\det X)\,X^{-T} = (\det X)\,X,$$

Therefore, A_{TT} is orthogonal. ∎

Lemma 2 $\begin{pmatrix} A_{\text{DD}} & A_{\text{LD}} \\ A_{\text{DL}} & A_{\text{LL}} \end{pmatrix}$ is orthogonal.
Proof: First, let us write down the entries:

$$A_{\text{DD}} = \begin{pmatrix} x_{11}^2 & x_{12}^2 & x_{13}^2 \\ x_{21}^2 & x_{22}^2 & x_{23}^2 \\ x_{31}^2 & x_{32}^2 & x_{33}^2 \end{pmatrix}, \quad A_{\text{DL}} = \sqrt{2}\begin{pmatrix} x_{21}x_{31} & x_{22}x_{32} & x_{23}x_{33} \\ x_{31}x_{11} & x_{32}x_{12} & x_{33}x_{13} \\ x_{11}x_{21} & x_{12}x_{22} & x_{13}x_{23} \end{pmatrix}$$

$$A_{\text{LD}} = \sqrt{2}\begin{pmatrix} x_{12}x_{13} & x_{13}x_{11} & x_{11}x_{12} \\ x_{22}x_{23} & x_{23}x_{21} & x_{21}x_{22} \\ x_{32}x_{33} & x_{33}x_{31} & x_{31}x_{32} \end{pmatrix},$$

$$A_{\text{LL}} = \begin{pmatrix} x_{33}x_{22} + x_{32}x_{23} & x_{31}x_{23} + x_{33}x_{21} & x_{32}x_{21} + x_{31}x_{22} \\ x_{13}x_{32} + x_{12}x_{33} & x_{11}x_{33} + x_{13}x_{31} & x_{12}x_{31} + x_{11}x_{32} \\ x_{23}x_{12} + x_{22}x_{13} & x_{21}x_{13} + x_{23}x_{11} & x_{22}x_{11} + x_{21}x_{12} \end{pmatrix}.$$

We need to prove that

$$A_{\text{DD}}^T A_{\text{DD}} + A_{\text{DL}}^T A_{\text{DL}} = A_{\text{LD}}^T A_{\text{LD}} + A_{\text{LL}}^T A_{\text{LL}} = I,$$

$$A_{\text{DD}}^T A_{\text{LD}} + A_{\text{DL}}^T A_{\text{LL}} = A_{\text{LD}}^T A_{\text{DD}} + A_{\text{LL}}^T A_{\text{DL}} = 0.$$

Denote $\mathbf{x}_1, \mathbf{x}_2, \mathbf{x}_3$ to be the three column vectors of X. Then, we have

$$A_{\text{DD}}^T A_{\text{DD}} + A_{\text{DL}}^T A_{\text{DL}} =$$

$$\begin{pmatrix} \|\mathbf{x}_1\|^4 & (\mathbf{x}_1 \cdot \mathbf{x}_2)^2 & (\mathbf{x}_1 \cdot \mathbf{x}_3)^2 \\ (\mathbf{x}_1 \cdot \mathbf{x}_2)^2 & \|\mathbf{x}_2\|^4 & (\mathbf{x}_2 \cdot \mathbf{x}_3)^2 \\ (\mathbf{x}_1 \cdot \mathbf{x}_3)^2 & (\mathbf{x}_2 \cdot \mathbf{x}_3)^2 & \|\mathbf{x}_3\|^4 \end{pmatrix} = \begin{pmatrix} 1 & 0 & 0 \\ 0 & 1 & 0 \\ 0 & 0 & 1 \end{pmatrix} = I,$$

$$A_{\text{LD}}^T A_{\text{LD}} + A_{\text{LL}}^T A_{\text{LL}} =$$

$$\begin{pmatrix} \|\mathbf{x}_2\|^2\|\mathbf{x}_3\|^2 & (\mathbf{x}_2 \cdot \mathbf{x}_3)(\mathbf{x}_3 \cdot \mathbf{x}_1) & (\mathbf{x}_2 \cdot \mathbf{x}_1)(\mathbf{x}_3 \cdot \mathbf{x}_2) \\ (\mathbf{x}_3 \cdot \mathbf{x}_2)(\mathbf{x}_1 \cdot \mathbf{x}_3) & \|\mathbf{x}_3\|^2\|\mathbf{x}_1\|^2 & (\mathbf{x}_3 \cdot \mathbf{x}_1)(\mathbf{x}_1 \cdot \mathbf{x}_2) \\ (\mathbf{x}_1 \cdot \mathbf{x}_2)(\mathbf{x}_2 \cdot \mathbf{x}_3) & (\mathbf{x}_1 \cdot \mathbf{x}_3)(\mathbf{x}_2 \cdot \mathbf{x}_1) & \|\mathbf{x}_1\|^2\|\mathbf{x}_2\|^2 \end{pmatrix} +$$

$$\begin{pmatrix} (\mathbf{x}_2 \cdot \mathbf{x}_3)^2 & (\mathbf{x}_2 \cdot \mathbf{x}_1)\|\mathbf{x}_3\|^2 & \|\mathbf{x}_2\|^2(\mathbf{x}_3 \cdot \mathbf{x}_1) \\ \|\mathbf{x}_3\|^2(\mathbf{x}_1 \cdot \mathbf{x}_2) & (\mathbf{x}_3 \cdot \mathbf{x}_1)^2 & (\mathbf{x}_3 \cdot \mathbf{x}_2)\|\mathbf{x}_1\|^2 \\ (\mathbf{x}_1 \cdot \mathbf{x}_3)\|\mathbf{x}_2\|^2 & \|\mathbf{x}_1\|^2(\mathbf{x}_2 \cdot \mathbf{x}_3) & (\mathbf{x}_1 \cdot \mathbf{x}_2)^2 \end{pmatrix} =$$

$$\begin{pmatrix} 1 & 0 & 0 \\ 0 & 1 & 0 \\ 0 & 0 & 1 \end{pmatrix} + \begin{pmatrix} 0 & 0 & 0 \\ 0 & 0 & 0 \\ 0 & 0 & 0 \end{pmatrix} = I,$$

$$A_{\text{DD}}A_{\text{DL}}^T + A_{\text{LD}}A_{\text{LL}}^T =$$

$$\sqrt{2}\begin{pmatrix} (\mathbf{x}_1 \cdot \mathbf{x}_2)(\mathbf{x}_1 \cdot \mathbf{x}_3) & (\mathbf{x}_1 \cdot \mathbf{x}_3)\|\mathbf{x}_1\|^2 & \|\mathbf{x}_1\|^2(\mathbf{x}_1 \cdot \mathbf{x}_2) \\ \|\mathbf{x}_2\|^2(\mathbf{x}_2 \cdot \mathbf{x}_3) & (\mathbf{x}_2 \cdot \mathbf{x}_3)(\mathbf{x}_2 \cdot \mathbf{x}_1) & (\mathbf{x}_2 \cdot \mathbf{x}_1)\|\mathbf{x}_2\|^2 \\ (\mathbf{x}_3 \cdot \mathbf{x}_2)\|\mathbf{x}_3\|^2 & \|\mathbf{x}_3\|^2(\mathbf{x}_3 \cdot \mathbf{x}_1) & (\mathbf{x}_3 \cdot \mathbf{x}_1)(\mathbf{x}_3 \cdot \mathbf{x}_2) \end{pmatrix} = 0,$$

$$A_{\mathrm{LD}}^T A_{\mathrm{DD}} + A_{\mathrm{LL}}^T A_{\mathrm{LD}} = \left(A_{\mathrm{DD}} A_{\mathrm{DL}}^T + A_{\mathrm{LD}} A_{\mathrm{LL}}^T \right)^T = 0. \qquad \blacksquare$$

Lemma 3 $\begin{pmatrix} A_{\mathrm{DD}} & A_{\mathrm{LD}} \\ A_{\mathrm{DL}} & A_{\mathrm{LL}} \end{pmatrix}$ commutes with $\begin{pmatrix} 0 & 1 & 1 & \\ 1 & 0 & 1 & 0 \\ 1 & 1 & 0 & \\ & 0 & & -I \end{pmatrix}$.

Proof: Note that A_{DD}, A_{DL}, A_{LD}^T all have $(1, 1, 1)^T$ as eigenvector with eigenvalues 1, 0, 0, respectively. Therefore,

$$A_{\mathrm{DD}} \begin{pmatrix} 0 & 1 & 1 \\ 1 & 0 & 1 \\ 1 & 1 & 0 \end{pmatrix} = A_{\mathrm{DD}} \left(\begin{pmatrix} 1 \\ 1 \\ 1 \end{pmatrix} (1, 1, 1) - I \right) =$$

$$\begin{pmatrix} 1 \\ 1 \\ 1 \end{pmatrix} (1, 1, 1) - A_{\mathrm{DD}} = \begin{pmatrix} 0 & 1 & 1 \\ 1 & 0 & 1 \\ 1 & 1 & 0 \end{pmatrix} A_{\mathrm{DD}},$$

$$A_{\mathrm{DL}} \begin{pmatrix} 0 & 1 & 1 \\ 1 & 0 & 1 \\ 1 & 1 & 0 \end{pmatrix} = A_{\mathrm{DL}} \left(\begin{pmatrix} 1 \\ 1 \\ 1 \end{pmatrix} (1, 1, 1) - I \right) = -A_{\mathrm{DL}},$$

$$\begin{pmatrix} 0 & 1 & 1 \\ 1 & 0 & 1 \\ 1 & 1 & 0 \end{pmatrix} A_{\mathrm{LD}} = \left(\begin{pmatrix} 1 \\ 1 \\ 1 \end{pmatrix} (1, 1, 1) - I \right) A_{\mathrm{LD}} = -A_{\mathrm{LD}}$$

$$\Rightarrow \begin{pmatrix} A_{\mathrm{DD}} & A_{\mathrm{LD}} \\ A_{\mathrm{DL}} & A_{\mathrm{LL}} \end{pmatrix} \begin{pmatrix} 0 & 1 & 1 & \\ 1 & 0 & 1 & 0 \\ 1 & 1 & 0 & \\ & 0 & & -I \end{pmatrix} = \begin{pmatrix} 0 & 1 & 1 & \\ 1 & 0 & 1 & 0 \\ 1 & 1 & 0 & \\ & 0 & & -I \end{pmatrix} \begin{pmatrix} A_{\mathrm{DD}} & A_{\mathrm{LD}} \\ A_{\mathrm{DL}} & A_{\mathrm{LL}} \end{pmatrix} =$$

$$\begin{pmatrix} 1 \\ 1 \\ 1 \\ 0 \\ 0 \\ 0 \end{pmatrix} \begin{pmatrix} 1 \\ 1 \\ 1 \\ 0 \\ 0 \\ 0 \end{pmatrix}^T - \begin{pmatrix} A_{\mathrm{DD}} & A_{\mathrm{LD}} \\ A_{\mathrm{DL}} & A_{\mathrm{LL}} \end{pmatrix} \qquad \blacksquare$$

E   GRADIENT AND HESSIAN OF ζ

Our function ζ is defined in Equation 13. The first and second derivatives are

$$\frac{d\zeta}{d\mu} = 2 \sum_i \left(f_i^S - f_i^E \right) \left(\frac{\partial f_i^S}{\partial \mu} + \frac{\partial f_i^S}{\partial u_i^F} \frac{\partial u_i^F}{\partial \mu} \right) =$$

$$= 2 \sum_i \left(f_i^S - f_i^E \right) \left(\frac{\partial f_i^S}{\partial \mu} + K_i^{CF} \frac{\partial u_i^F}{\partial \mu} \right),$$

$$\frac{d^2\zeta}{d^2\mu} = 2 \sum_i \left(\frac{\partial f_i^S}{\partial \mu} + \frac{\partial f_i^S}{\partial u_i^F} \frac{\partial u_i^F}{\partial \mu} \right)^T \left(\frac{\partial f_i^S}{\partial \mu} + \frac{\partial f_i^S}{\partial u_i^F} \frac{\partial u_i^F}{\partial \mu} \right) +$$

$$+ 2 \sum_i \left(f_i^S - f_i^E \right) \left(\frac{\partial^2 f_i^S}{\partial \mu^2} + 2 \frac{\partial^2 f_i^S}{\partial \mu \partial u_i^F} \frac{\partial u_i^F}{\partial \mu} + \right.$$

$$\left. + \left(\frac{\partial u_i^F}{\partial \mu} \right)^T \frac{\partial^2 f_i^S}{\partial u_i^{F2}} \left(\frac{\partial u_i^F}{\partial \mu} \right) + \frac{\partial f_i^S}{\partial u_i^F} \frac{\partial^2 u_i^F}{\partial \mu^2} \right).$$

The gradient and Hessian of displacements with respect to μ can be derived from the force equilibrium equation $f^F \left(\mu, u^F(\mu) \right) \equiv 0$,

$$\frac{df^F}{d\mu} = \frac{\partial f^F}{\partial \mu} + \frac{\partial f^F}{\partial u^F} \frac{\partial u^F}{\partial \mu} =$$

$$= \frac{\partial f^F}{\partial \mu} + K^{FF} \frac{\partial u^F}{\partial \mu} = 0 \; \Rightarrow \; \frac{\partial u^F}{\partial \mu} = - \left(K^{FF} \right)^{-1} \frac{\partial f^F}{\partial \mu},$$

$$\frac{d^2 f^F}{d\mu^2} = \frac{\partial^2 f^F}{\partial \mu^2} + 2 \frac{\partial^2 f^F}{\partial \mu \partial u^F} \frac{\partial u^F}{\partial \mu} + \left(\frac{\partial u^F}{\partial \mu} \right)^T \frac{\partial^2 f^F}{\partial u^{F2}} \left(\frac{\partial u^F}{\partial \mu} \right) + \frac{\partial f^F}{\partial u^F} \frac{\partial^2 u^F}{\partial \mu^2} =$$

$$= 2 \frac{\partial K^{FF}}{\partial \mu} \frac{\partial u^F}{\partial \mu} + \left(\frac{\partial u^F}{\partial \mu} \right)^T \frac{\partial K^{FF}}{\partial u^F} \left(\frac{\partial u^F}{\partial \mu} \right) + K^{FF} \frac{\partial^2 u^F}{\partial \mu^2} = 0$$

$$\Rightarrow \frac{\partial^2 u^F}{\partial \mu^2} = - \left(K^{FF} \right)^{-1} \left(2 \frac{\partial K^{FF}}{\partial \mu} + \left(\frac{\partial u^F}{\partial \mu} \right)^T \frac{\partial K^{FF}}{\partial u^F} \right) \left(\frac{\partial u^F}{\partial \mu} \right).$$

The elastic energy, force, tangent stiffness matrix, and their gradients with respect to μ are

$$E \left(\mu, u(\mu) \right) = 2\pi \sum_k w_k r_k \Psi \left(\mu, F_k \right),$$

$$f \left(\mu, u(\mu) \right) = \left(\frac{\partial E}{\partial u} \right)^T = 2\pi \sum_k \omega_k r_k \left(\frac{\partial F_k}{\partial u} \right)^T \left(\frac{\partial \Psi}{\partial F} _{|F=F_k} \right)^T,$$

$$\frac{\partial f}{\partial \mu} = 2\pi \sum_k \omega_k r_k \left(\frac{\partial F_k}{\partial u} \right)^T \frac{\partial^2 \Psi}{\partial F \partial \mu} _{|F=F_k},$$

$$K \left(\mu, u(\mu) \right) = \frac{\partial^2 E}{\partial u^2} = 2\pi \sum_k \omega_k r_k \left(\frac{\partial F_k}{\partial u} \right)^T \frac{\partial^2 \Psi}{\partial F^2} _{|F=F_k} \left(\frac{\partial F_k}{\partial u} \right),$$

$$\frac{\partial K}{\partial \mu} = 2\pi \sum_k \omega_k r_k \left(\frac{\partial F_k}{\partial u} \right)^T \frac{\partial^3 \Psi}{\partial F^2 \partial \mu} _{|F=F_k} \left(\frac{\partial F_k}{\partial u} \right),$$

$$\frac{\partial K}{\partial u} = \frac{\partial^3 E}{\partial u^3} = 2\pi \sum_k \omega_k r_k \left(\frac{\partial F_k}{\partial u} \right)^T \frac{\partial^3 \Psi}{\partial F^3} _{|F=F_k} \left(\frac{\partial F_k}{\partial u} \right) \left(\frac{\partial F_k}{\partial u} \right).$$

Note that the weights ω_k were defined in Section 4.2. Equations 14 and 15 now follow by discarding the 3rd-order derivatives of ψ. This did not impede our optimization; and actually, we found that useful optimizations can be obtained even with as little as (but not without) the first tensor product term of $d^2\zeta/d\mu^2$ (i.e., the term appearing in the first line of the above expression for $d^2\zeta/d\mu^2$).